



Defence Research and  
Development Canada

Recherche et développement  
pour la défense Canada

Copy No:



# **Comparative analysis of behind armour debris from shaped charge impacts on aluminium and steel targets**

Alexandra Sirois  
Yves Baillargeon  
Alexandre Vallée  
Guy Bergeron  
DRDC Valcartier

**Defence R&D Canada – Valcartier**

Technical Report  
DRDC Valcartier TR 2012-063  
June 2012

**Canada** 

# **Comparative analysis of behind armour debris from shaped charge impacts on aluminium and steel targets**

Alexandra Sirois  
Yves Baillargeon  
Alexandre Vallée  
Guy Bergeron  
DRDC Valcartier

**Defence R&D Canada – Valcartier**

Technical Report

DRDC Valcartier TR 2012-063

June 2012

Principal Author

*Original signed by Alexandra Sirois*

---

Alexandra Sirois

Protection and Weapons Effects Section

Approved by

*Original signed by Dennis Nandlall*

---

Dennis Nandlall

Section Head- Protection and Weapons Effects Section

Approved for release by

*Original signed by Christian Carrier*

---

Christian Carrier

Chief Scientist

© Her Majesty the Queen in Right of Canada, as represented by the Minister of National Defence, 2012

© Sa Majesté la Reine (en droit du Canada), telle que représentée par le ministre de la Défense nationale, 2012

## Abstract

---

This report aims at comparing the Behind Armour Debris (BAD) generated by the penetration of a shaped charge jet into two common vehicle armour materials: 5083 aluminium alloy and Rolled Homogeneous Armour (RHA) steel.

A statically detonated 66 mm shaped charge was used for the tests, which took place at the DRDC Valcartier exterior ranges. Targets were tested for thicknesses between 1.6 mm and 127.5 mm for RHA and 13 mm to 133 mm for 5083 aluminium alloy. Witness packs were used to record the behind armour debris, then scanned and analysed to obtain the behind armour debris distributions (fragment position, mass, velocity and lethality).

Comparing number of fragments versus thickness, aluminium has shown to produce about 60% less fragments around 13 mm. This difference gradually goes down to twice less for the thickest targets. Number of BAD in RHA reaches a peak around 12 mm ( $94 \text{ kg/m}^2$ ) then decreases with thickness. For aluminium, targets thinner than 13 mm ( $35 \text{ kg/m}^2$ ) were not tested, therefore the exact location of the peak in BAD is not visible in the test results, but from 13 mm to 127.5 mm, a gradual decrease in BAD was found. The fragment mass and velocity distributions are similar for both materials, but since aluminium produces fewer fragments, the lethality of the debris cone is smaller for aluminium. Predictive equations to numerically reproduce the behind armour debris distributions were developed based on the test results and are presented.

The behind armour debris characterisation data was consolidated into probability distribution models to be implemented into vulnerability-lethality tools. This was needed to estimate the vulnerability of personnel inside vehicles composed of any of those two materials when subjected to the shaped charge threat.

## Résumé

---

Les débris derrière le blindage résultant d'impacts de charges creuses dans deux matériaux fréquemment utilisés pour le blindage de véhicules (l'acier de blindage RHA et l'alliage d'aluminium 5083) sont comparés ici.

Les tirs consistaient en des détonations statiques de charges creuses de 66 mm sur les sites d'essai de RDDC Valcartier. Les épaisseurs de cibles étaient entre 1,6 mm et 127,5 mm pour le RHA, et entre 13 mm et 133 mm pour l'aluminium. Des panneaux témoins ont été utilisés pour enregistrer les débris derrière le blindage puis scannés et analysés pour obtenir les distributions de débris (position, masse, vitesse et létalité des fragments).

L'analyse du nombre de fragments par rapport à l'épaisseur a montré que, dans tous les cas, l'aluminium produit environ 60 % moins de fragments que le RHA. Les distributions de masses et de vitesses sont similaires pour les deux matériaux, mais en produisant moins de fragments pour la même épaisseur, la zone de létalité produite par le cône de débris est plus petite pour l'aluminium. Des équations prédictives, qui serviront à reproduire numériquement les nuages de

débris, ont été développées et sont présentées dans ce rapport. Elles sont basées sur les résultats expérimentaux.

La caractérisation des débris derrière le blindage a été consolidée en un modèle de distribution de probabilité afin d'être implémentée dans les outils de vulnérabilité-létalité. Cela est nécessaire pour pouvoir évaluer la vulnérabilité du personnel à l'intérieur de véhicules composés de ces matériaux lorsque exposés à un impact de charge creuse.

## Executive summary

---

### Comparative analysis of behind armour debris from shaped charge impacts on aluminium and steel targets:

**Alexandra Sirois; Yves Baillargeon; Alexandre Vallée; Guy Bergeron; DRDC Valcartier TR 2012-063; Defence R&D Canada – Valcartier; June 2012.**

**Introduction or background:** The present report aims at comparing the Behind Armour Debris (BAD) generated by the penetration of a shaped charge jet into two common vehicle armour materials: 5083 aluminium alloy and Rolled Homogeneous Armour (RHA) steel.

A 66 mm shaped charge was used for the tests. All tests were static and took place at the DRDC Valcartier exterior ranges between 2002 and 2004. RHA targets were tested for thicknesses between 1.6 mm and 127.5 mm. Aluminium 5083 targets were tested for thicknesses between 13 mm and 133 mm.

Witness packs were used to record the behind armour debris. After the tests, all witness packs were scanned and analysed to obtain the behind armour debris distributions (fragment position, mass, velocity and lethality).

**Results:** Looking at the number of fragments versus thickness, in all cases aluminium produced a lower number of behind armour debris by approximately 60%. The fragment mass and velocity distributions are similar for both materials, but since aluminium produces fewer fragments for the same thickness and areal density, the lethality of the debris cone is also more restrained for aluminium. The behind armour debris characterisation data was consolidated into a predictive model ready for implementation into vulnerability-lethality tools.

**Significance:** The behind armour debris characterisation and predictive model shown in this report are needed to estimate the vulnerability of personnel inside vehicles composed of those two materials when subjected to the shaped charge threat.

**Future plans:** Behind armour debris characterisation should be made using novel vehicle materials, including transparent armour. Improvements will be made to the behind armour analysis tool DeCaM to speed up the analysis. Finally, additional experimental tests would help to refine the BAD versus thickness predictive model.

## Sommaire

---

### Comparative analysis of behind armour debris from shaped charge impacts on aluminium and steel targets:

Alexandra Sirois; Yves Baillargeon; Alexandre Vallée; Guy Bergeron; DRDC Valcartier TR 2012-063; R & D pour la défense Canada – Valcartier; Juin 2012.

**Introduction ou contexte:** Les débris derrière le blindage résultant d'impacts de charges creuses dans deux matériaux fréquemment utilisés pour blindages de véhicules (l'acier de blindage RHA et l'alliage d'aluminium 5083) sont comparés.

Une charge creuse de 66 mm a été utilisée pour les tests. Tous les tirs étaient statiques. Les tests ont été effectués sur les sites d'essais de RDDC Valcartier entre 2002 et 2004. L'acier a été testé pour des épaisseurs entre 1,6 mm et 127,5 mm. L'alliage d'aluminium 5083 a été testé pour des épaisseurs entre 13 mm et 133 mm.

Des panneaux témoins ont été utilisés pour enregistrer les débris. Après les tests, tous les panneaux témoins ont été scannés et analysés pour obtenir les distributions de débris (position, masse, vitesse et létalité des fragments).

**Résultats:** L'analyse du nombre de fragments par rapport à l'épaisseur a montré que, dans tous les cas, l'aluminium produit une moins grande quantité de fragments (environ 60 % moins de fragments). Les distributions de masses et de vitesses sont similaires pour les deux matériaux, mais en produisant moins de fragments pour la même épaisseur, la zone de létalité produite par le cône de débris est plus petite pour l'aluminium. Toutes les données de caractérisation de débris ont permis de développer un modèle prédictif prêt pour implémentation dans les outils de vulnérabilité-létalité.

**Importance:** La caractérisation des débris derrière le blindage et le modèle prédictif présentés dans ce rapport sont nécessaires pour estimer la vulnérabilité du personnel à l'intérieur de véhicules composés de ces matériaux lorsqu'exposés à la menace de charges creuses.

**Perspectives:** Des caractérisations de débris derrière le blindage devraient être faites pour les matériaux de blindage émergents, incluant les blindages transparents. Des améliorations à l'outil d'analyse de panneaux témoins DeCaM devraient être effectuées afin de rendre l'analyse plus efficace. Finalement, des données expérimentales additionnelles permettraient de raffiner le modèle prédictif de débris par rapport à l'épaisseur.

# Table of contents

---

Abstract .....	i
Résumé .....	i
Executive summary .....	iii
Sommaire .....	iv
Table of contents .....	v
List of figures .....	vi
List of tables .....	viii
1 .... Introduction.....	1
2 .... Test Materials .....	3
2.1    Ammunition.....	3
2.2    Targets .....	3
3 .... Test setup .....	5
4 .... Test results and discussion.....	7
4.1    Total number of fragments .....	7
4.2    Fragment mass and velocity .....	10
4.2.1    Fragment Mass and velocity calculation for steel fragments .....	10
4.2.2    Correction for aluminium fragments.....	11
4.2.3    Fragment Mass.....	11
4.2.4    Fragment velocity .....	13
4.2.5    Discussion on high velocities.....	16
4.3    Fragment spatial distribution .....	18
4.4    Fragment lethality.....	20
4.4.1    Calculation of the Percentage of Incapacitation (PI) .....	20
4.4.2    Percentage of incapacitation results .....	23
5 .... Data consolidation into a vulnerability model .....	27
5.1    Data parameterization.....	27
5.1.1    Cumulative mass distribution.....	27
5.1.2    Cumulative energy distribution .....	28
5.1.3    Expected total mass and energy .....	37
5.1.4    Fragment spatial distribution.....	40
5.2    Fragment table set up.....	45
5.3    Further improvements .....	48
6 .... Conclusion .....	51
7 .... References .....	53
Annex A .. Total and average number of fragments .....	55



## List of figures

---

Figure 1: Test setup .....	5
Figure 2: Total number of fragments from experiments and equation .....	9
Figure 3: Total number of fragments versus areal density .....	9
Figure 4: Average mass distributions for aluminium targets from 13 to 133 mm.....	11
Figure 5: Average mass distributions for RHA targets from 1.6 to 127.5 mm .....	12
Figure 6: Normalised mass distribution for all thicknesses tested .....	12
Figure 7: Cumulative mass distributions for aluminium targets from 13 to 133 mm .....	13
Figure 8: Cumulative mass distributions for RHA targets from 1.6 to 127.5 mm .....	13
Figure 9: Normalised fragment velocity distributions for aluminium targets from 13 to 133 mm thicknesses .....	14
Figure 10: Normalised fragment velocity distributions for RHA targets from 1.6 to 127.5 mm thicknesses.....	14
Figure 11: Normalised velocity distributions for all thicknesses tested .....	16
Figure 12: Behind armour debris cloud for velocity measurements.....	17
Figure 13: Velocity measurements (pictures and from WPAS) versus azimuth angle .....	18
Figure 14: Geometry of BAD cones.....	19
Figure 15: Experimental distribution of the BAD versus azimuth angle for Al ( $d\theta = 1^\circ$ ) .....	19
Figure 16: Experimental distribution of the BAD versus azimuth for RHA ( $d\theta = 1^\circ$ ).....	20
Figure 17: Schematic top view of vehicle impacted by a shaped charge .....	21
Figure 18: Side view and close-up of exposed surface area .....	21
Figure 19: Area for PHit calculation .....	23
Figure 20: Percentages of incapacitation for RHA.....	24
Figure 21: Percentages of incapacitation for aluminium.....	24
Figure 22: PI for 13 mm Al, 12 mm RHA and 44.5 mm aluminium .....	25
Figure 23: Experimental cumulative mass distributions of BAD for RHA plates 1.6 mm and 12 mm thick along with fit from equations 12 and 13 .....	29
Figure 24: Experimental cumulative mass distributions of BAD for RHA plates 25.5 mm and 127.5 mm thick along with fit from equations 12 and 13 .....	30
Figure 25: Experimental cumulative mass distributions of BAD for Al plates 13 mm and 44.5 mm thick along with fit from equations 12 and 14 .....	31
Figure 26: Experimental cumulative mass distributions of BAD for Al plates 89 mm and 133 mm thick along with fit from equations 12 and 14 .....	32

Figure 27: Experimental cumulative energy distributions of BAD for RHA plates 1.6 mm and 12 mm thick along with fit from equations 15 and 16 .....	33
Figure 28: Experimental cumulative energy distributions of BAD for RHA plates 25.5 mm and 127.5 mm thick along with fit from equations 15 and 16.....	34
Figure 29: Experimental cumulative energy distributions of BAD for Al plates 13 mm and 44.5 mm thick along with fit from equations 15 and 17 .....	35
Figure 30: Experimental cumulative energy distributions of BAD for Al plates 89 mm and 133 mm thick along with fit from equations 15 and 17 .....	36
Figure 31: Expected total mass (top) and total energy (bottom) of fragments as a function of the target thickness T for RHA with fits from equations 19, 20, 22 and 23.....	38
Figure 32: Expected total mass (top) and total energy (bottom) of fragments as a function of the target thickness T for Al with fits from equations 19, 21, 22 and 24 .....	39
Figure 33: Experimental distribution of the BAD as a function of the azimuth opening for RHA (top) and Al (bottom).....	41
Figure 34: PDF for azimuth BAD distribution for Al plates 13 mm (top) and 44.5 mm (bottom) thick.....	43
Figure 35: PDF for azimuth BAD distribution for Al plates 89 mm (top) and 133 mm (bottom) thick.....	44
Figure 36: Illustration of domains in a distribution (e.g. cumulative) for a variable $x$ .....	45

## List of tables

---

Table 1: Target description.....	4
Table 2: Average number of fragments.....	7
Table 3: Average and standard deviation of fragment velocity.....	15
Table 4: Fragment velocities measured on X-ray.....	17
Table A-1: Total number of fragments for the Al5083 targets.....	55
Table A-2: Total number of fragments for the RHA targets.....	56

# 1 Introduction

---

The present report aims at comparing the Behind Armour Debris (BAD) generated by the penetration of a shaped charge jet into two common vehicle armour materials: 5083 aluminium alloy and Rolled Homogeneous Armour (RHA) steel. It also aims at presenting the predictive equations that were developed to numerically reproduce behind armour debris clouds for these two materials for a range of thicknesses. The equations are to be used in Vulnerability-Lethality (VL) models to estimate the vulnerability of personnel inside vehicles composed of those two materials when subjected to the shaped charge threat.

A 66 mm shaped charge was used for the tests. All tests were static and took place at the DRDC Valcartier exterior ranges. RHA targets were tested for thicknesses between 1.6 mm and 127.5 mm (between  $13 \text{ kg/m}^2$  and  $1001 \text{ kg/m}^2$  in areal density). 5083 aluminium alloy targets were tested for thicknesses between 13 mm and 133 mm (between  $35 \text{ kg/m}^2$  and  $354 \text{ kg/m}^2$  in areal density).

Witness packs were used to record the behind armour debris. After the tests, all witness packs were scanned and analysed to obtain the behind armour debris distributions (fragment position, mass, velocity and lethality). An algorithm was developed to calculate fragment mass and velocity. The penetration model used in the algorithm is the THOR penetration model. A modification to the THOR penetration model was made to be able to analyse fragments from materials other than steel (in this case: aluminium). This modification is based on the hypothesis that the energy required to penetrate a target is constant regardless of the penetrator material.

In this report, the test materials are first presented (ammunition and targets). The test setup is then explained. To compare the behind armour debris coming from shaped charge impacts on RHA and aluminium, the total number of fragments are first presented. The algorithm and penetration model are presented along with the modification that was done to the model to analyse fragments from materials other than steel. This is followed by the mass and velocity distributions. Finally, the method for calculation of the Probabilities of Incapacitation (PI) from BAD is presented, followed by the PI results and analysis.

This page intentionally left blank.

## **2 Test Materials**

---

### **2.1 Ammunition**

The shaped charges used contained a 44° copper cone liner and had a diameter of approximately 65 mm.

### **2.2 Targets**

5083 aluminium alloy (MIL-DTL-46027) and Rolled Homogeneous Armour (RHA) steel (MIL-A-12560) plates were used for the tests. Table 1 shows the details of the targets and number of shots for each.

Some thicknesses were achieved by stacking multiple thinner plates, such as the 133.5 mm thick aluminium condition performed with three 44.5 mm plates. This was based on the assumption that a stack of plates behaves the same as single a plate of the given thickness.

*Table 1: Target description*

<b>Target material</b>	<b>Target configuration</b>	<b>Total target thickness (mm)</b>	<b>Areal density (kg/m<sup>2</sup>)</b>	<b>Number of shots</b>
Al 5083	1 x 12.7 mm	13	35	4
	1 x 44.5 mm	44.5	118	3
	2 x 44.5 mm	89	237	3
	3 x 44.5 mm	133.5	355	3
RHA	1 x 1.6 mm	1.6	13	3
	1 x 6 mm	6	47	3
	2 x 6 mm	12	94	3
	3 x 6 mm	18	141	3
	1 x 18 mm	18	141	3
	1 x 25.5 mm	25.5	200	3
	2 x 25.5 mm	51	400	3
	5 x 25.5 mm	127.5	1001	3

### 3 Test setup

Figure 1 shows a side view of the test setup. The shaped charge is shot downwards. The targets were placed on target table. The center of the table is opened and the target plates were centred on the opening. For each test, a shaped charge was placed on top of the target plate. The shaped charge was detonated statically at 0° obliquity. Polystyrene was used to elevate the shaped charge at its built-in standoff of 13.2 cm. For each test, one witness pack was used to record the behind armour debris. The witness packs consisted of 1 mm, 1 mm and 3 mm thick Al-1100 plate and one 1.5 mm thick AISI 1010-1020 steel plate. Each witness pack was located 600 mm behind the back of the target plate.

After the tests, each plate of the witness packs was scanned and analysed using the semi-automatic Witness Pack Analysis System (WPAS) [1]. WPAS provides the position and area of the holes on each sheet of the witness pack. The software DeCaM is then used to analyse the data. For each shot, the WPAS output files from each sheet of the witness pack are loaded in DeCaM. Matches are then made between the hole position on each plate to track the fragment's path through the witness pack. The fragment mass and velocities are then estimated using a penetration model. The penetration model and algorithm used in DeCaM is explained in detail in subsection 4.2.1

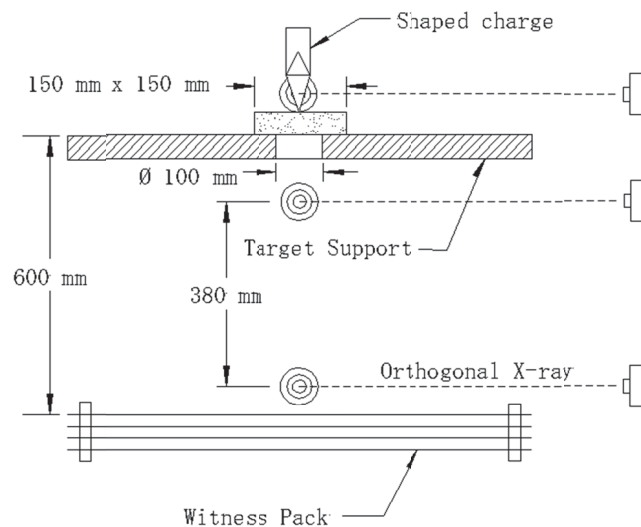


*Figure 1: Test setup*



This page intentionally left blank.

## 4 Test results and discussion

---

### 4.1 Total number of fragments

Table 2 shows the average number of fragments versus thickness and areal density for the two target materials. Table A- and Table A- in annex A show the details. As seen in previous tests [5] on steel targets the number of behind armour debris reaches a peak at the critical thickness of 12 mm. Aluminium produces a lower number of fragments than steel for all the tested areal densities, but additional tests on thinner plates would be needed to evaluate the critical thickness for aluminium.

*Table 2: Average number of fragments*

	<b>Thickness (mm)</b>	<b>Areal density (kg/m<sup>2</sup>)</b>	<b>Average number of fragments</b>
Al 5083	13	35	408
	44.5	118	300
	89	237	136
	133.5	355	79
RHA	1.6	13	748
	6	47	956
	12	94	1165
	18	141	1087
	25.5	200	981
	51	400	666
	127.5	1001	156

Equation (1), developed by Merendino and al., and further modified in [5] estimates the total number of fragments for a shaped charge hitting a metallic target.

$$N(T) = K \left[ \frac{\delta}{1 + \delta} \frac{\pi d_j^{1.62} \rho_j V_j^4}{8 Z_0} \right] \left( \frac{Z_0}{Z_0 + T} \right)^{4\delta+1} \quad (1)$$

Where N is the number of fragments, T is the target thickness (m),  $K = 1.5 \times 10^{-8} \text{ s/J}$ ,  $d_j$  is the jet diameter at breakup (m),  $\rho_j$  is the jet density ( $\text{kg/m}^3$ ),  $V_j$  (m/s) is the jet tip velocity (m/s),  $Z_0$  is the standoff between the copper cone and the target (0.132 m) and  $\delta = \rho_j/\rho_t$ .  $\rho_t$  is the target density ( $\text{kg/m}^3$ ).

This equation was modified to account for the drop in number of fragments at critical thickness for thin targets using experimental tests against steel targets. The equation was modified using a Mott distribution [5] based on scaled shaped charge tests. The corrected number of fragments ( $N_M(T)$ ) is estimated:

$$N_M(T) = K_{steel} N(0.012) d_{cone} \frac{\beta}{\alpha} \left( \frac{T}{\alpha} \right)^{\beta-1} e^{-(T/\alpha)^\beta} \quad (2)$$

Where  $K_{steel}$  is a factor based on experimental fitting, it is equal to 1219 for steel.  $N(0.012)$  in equation (1) applied to the critical thickness 0.012 m.  $D_c$  is the cone diameter (m),  $\alpha = 937$  and  $\beta = 1.15$ .

Figure 2 shows the number of fragments versus thickness for the two materials tested along with the predictive equation plots. The predictive equation for RHA overestimates the number of fragments. Factor K was fitted for aluminium targets based on the experimental data shown here where  $K_{Al} = 622$ .

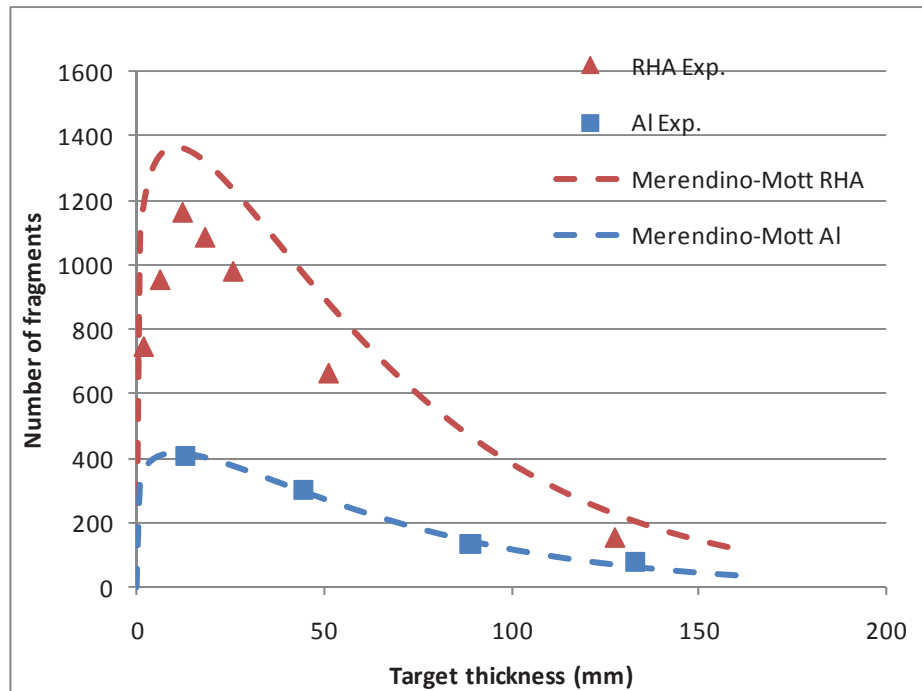


Figure 2: Total number of fragments from experiments and equation

Figure 3 shows the total number of fragments versus areal density. For the same areal density, the number of fragments created upon impact of the shaped charge jet is lower for aluminium targets than the RHA targets in all the thicknesses tested.

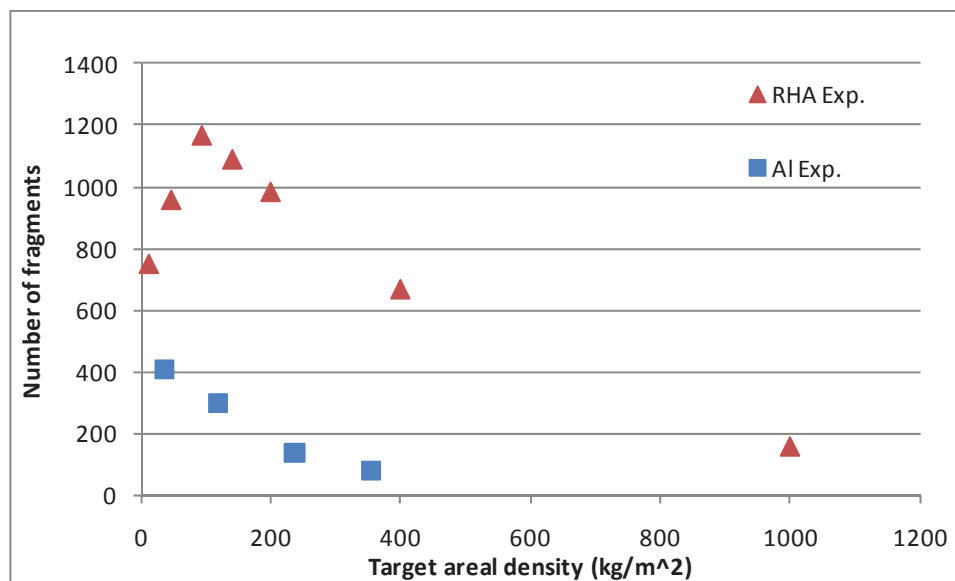


Figure 3: Total number of fragments versus areal density

## 4.2 Fragment mass and velocity

### 4.2.1 Fragment Mass and velocity calculation for steel fragments

Fragment mass and velocities were calculated using an algorithm implemented in DeCaM. The algorithm uses the THOR empirical penetration model. Two empirical equations from the THOR model are used in the algorithm:

The first equation calculates the residual velocity  $V_r$  (ft/s) of a projectile/fragment impacting a target at striking velocity  $V_s$  (ft/s):

$$V_r = V_s - 10^c(hA)^\alpha m_s^\beta (\sec \omega)^\gamma V_s^\lambda \quad (3)$$

The second equation calculates the velocity  $V_0$  (ft/s) for a projectile/fragment to just penetrate a plate of a certain thickness:

$$V_0 = 10^{c1}(hA)^{\alpha1} m_s^{\beta1} (\sec \omega)^{\lambda1} \quad (4)$$

Where  $m_s$  the projectile initial mass (grain),  $h$  is the target thickness (inch). In this case, it is the witness plate thickness,  $A$  is the area of the hole in the target plate (inch<sup>2</sup>),  $\omega$  is the angle of the shot with respect to normal of the target and  $c, \alpha, \beta, \gamma, \lambda$  are constants related to the target material.

For these tests, the witness packs were made up of four witness plates. Each fragment penetrated a number of these witness plates, and its trajectory is recorded by the holes made on each penetrated plate.

In the algorithm, the fragment mass is assumed to stay constant throughout penetration of the witness pack. The fragment mass  $m_s$  is calculated as:

$$m_s = \left( \frac{A_{plate\ 1}}{K} \right)^{3/2} \quad (5)$$

In this equation,  $A_{plate\ 1}$  is the area of the hole created on the first plate of the witness pack by the fragment.  $K$  is the fragment shape factor. A fixed fragment shape factor is used ( $K=0.005\text{ m}^2/\text{kg}^{2/3}$ ). Fragment shape factors from shaped charge impacts on steel plates have not been measured experimentally. The fragment shape factor used is for forged steel fragments from fragmenting warheads [3]. It is assumed that all the fragments recorded are made of material from the target, and not from the copper shaped charge jet. In reality, there are a small number of fragments that are made of the copper jet material, but it is impossible to discern them from the fragments from the target when using witness packs, because they record holes and not the fragments themselves.

The algorithm begins the calculations at the last plate perforated (plate  $n$ ) on the witness pack. It calculates the impact velocity  $V_{0\ n}$  needed to just penetrate this plate  $n$ .

The algorithm then goes to the preceding plate (plate  $n-1$ ) and calculates the striking velocity  $V_s^{n-1}$  needed to penetrate this plate with a residual velocity  $V_r^{n-1} = V_{0\ n}$ . This goes on all the way to the first plate.

It then does the same calculations assuming plate n+1 was just at the limit of being penetrated. The velocity associated with each fragment is the average of striking velocity at the first plate needed to penetrate n plates and n+1 plates.

## 4.2.2 Correction for aluminium fragments

The THOR model was developed for steel fragments. A modification was done to be able to use THOR for aluminium fragments. Throughout the THOR algorithm, the fragment is assumed to be steel. At the end of the calculation, the energy conservation principle is used to make the correction to other fragment materials, using equations (6) and (7). This method assumes that the volume of the fragment recorded as a hole in the witness pack and the energy of the fragment required to penetrate the witness pack are the same regardless of the fragment material.

$$m_{Al\ fragment} = \frac{\rho_{Al}}{\rho_{Steel}} m_{steel\ fragment} \quad (6)$$

$$V_{Al\ fragment} = \frac{V_{steel\ fragment}}{\sqrt{\frac{\rho_{Al}}{\rho_{Steel}}}} \quad (7)$$

## 4.2.3 Fragment Mass

The smallest hole area calculated using the WPAS is 0.004 cm<sup>2</sup>. This corresponds to a mass of 0.000716 g for a steel and 0.000246 g for an aluminium fragment. Those fragments have a very small mass, but still need to be considered in the analysis because they have enough energy to penetrate at least the first plate of the witness pack, therefore have the potential of causing injury.

Fragment mass distributions are shown for Al and RHA targets in Figures 4 and 5.

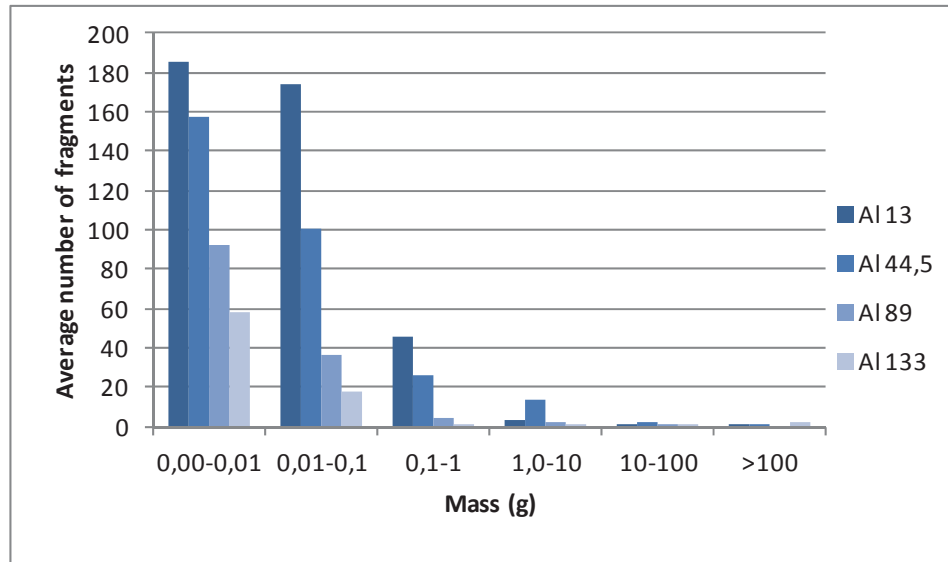


Figure 4: Average mass distributions for aluminium targets from 13 to 133 mm

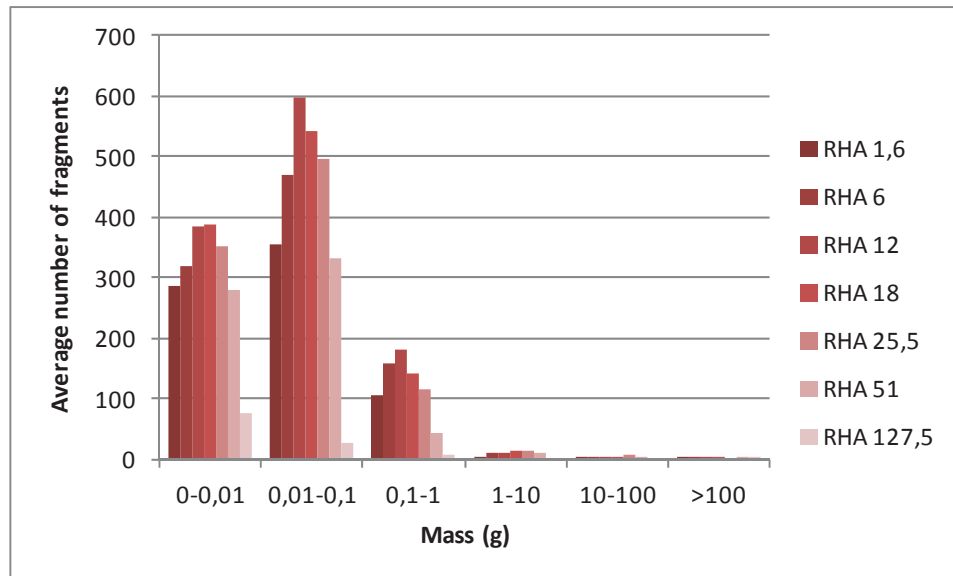


Figure 5: Average mass distributions for RHA targets from 1.6 to 127.5 mm

Figure 6 shows the normalised mass distribution for all thicknesses combined, and for the two materials tested. The normalised data shows a larger proportion of heavier fragments for RHA: 52% of aluminium fragments are between 0 and 0.01 g, whereas 49% are between 0.01 and 0.1 g for RHA. This is predictable because steel (RHA) is denser than aluminium and the mass of the aluminium fragments was calculated, as explained in Subsection 4.2.2, based on the assumption that the fragment that perforates a hole of a specific area in a witness plate has a constant volume, regardless of the fragment material.

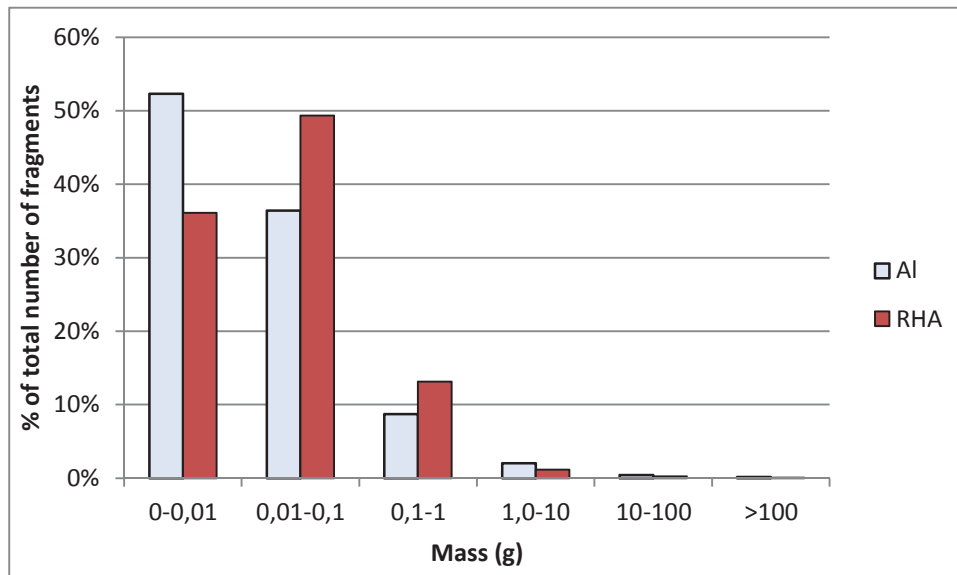


Figure 6: Normalised mass distribution for all thicknesses tested

Figures 6 and 7 show the cumulative fragment distributions. This data is further analysed in Subsection 5.1.3.

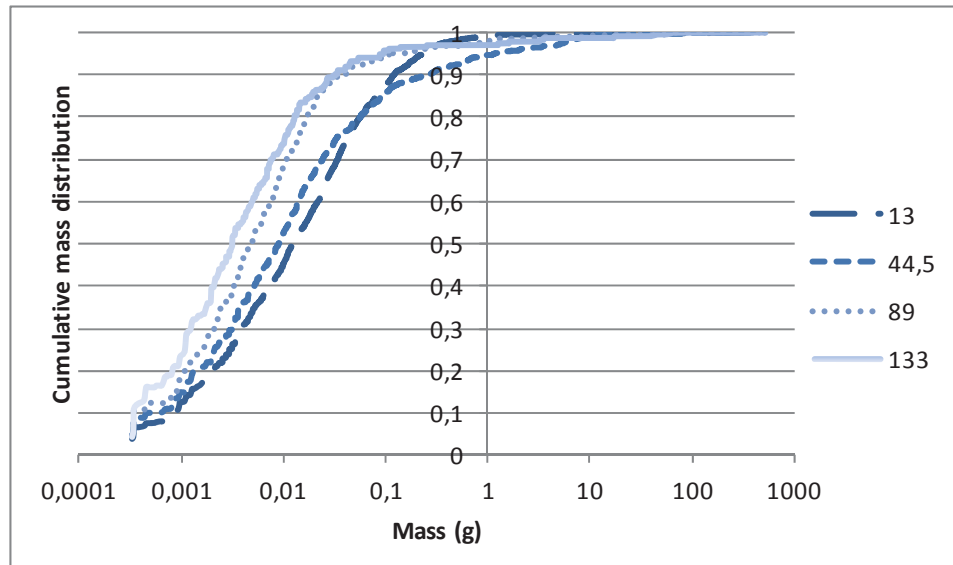


Figure 7: Cumulative mass distributions for aluminium targets from 13 to 133 mm

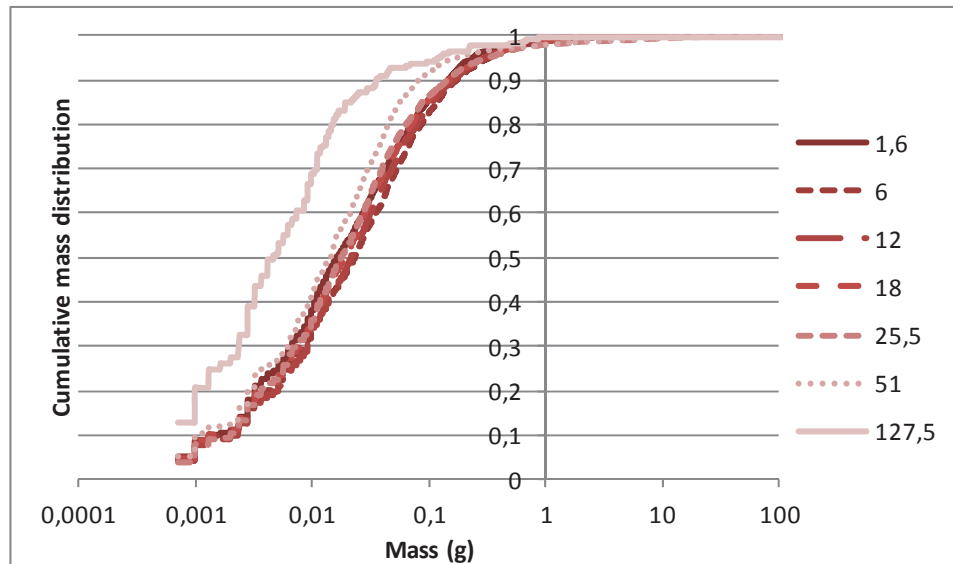


Figure 8: Cumulative mass distributions for RHA targets from 1.6 to 127.5 mm

#### 4.2.4 Fragment velocity

Figures 9 and 10 show the normalised fragment velocity distributions for aluminium and RHA targets. The normalisation is done over the total number of fragments for each thickness. Table 3 shows the fragment velocity statistics. The fragment velocity distribution seems to be dependent



on the thickness for the aluminium targets, with the most common velocity bracket shifting from 1000 - 1500 m/s at 13 mm to 2500 - 3000 m/s at 133 mm and average velocity increasing with thickness. The fragment velocity distributions do not seem to be dependent on the thickness for the RHA targets, with the most common velocities in the 1000 - 1500 m/s bracket.

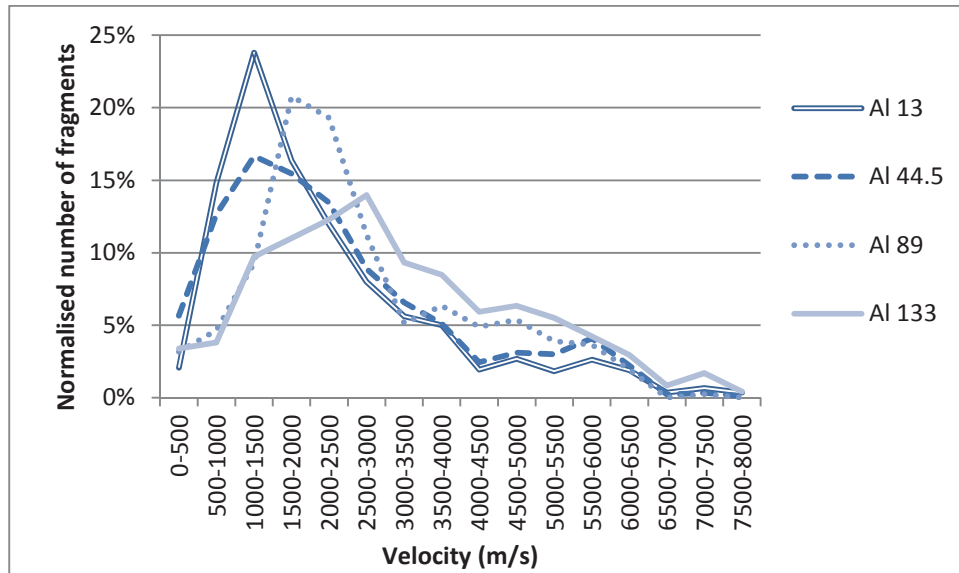


Figure 9: Normalised fragment velocity distributions for aluminium targets from 13 to 133 mm thicknesses

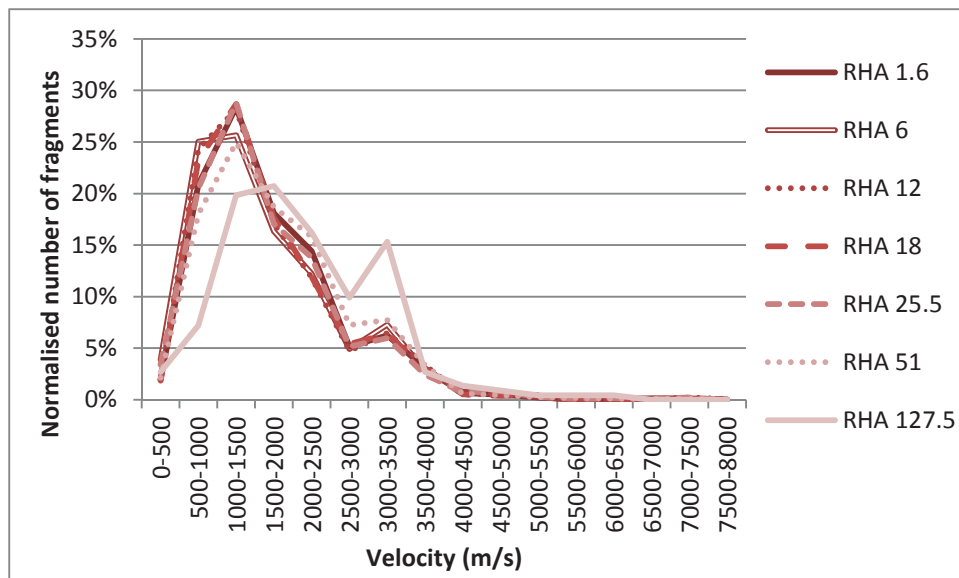


Figure 10: Normalised fragment velocity distributions for RHA targets from 1.6 to 127.5 mm thicknesses

*Table 3: Average and standard deviation of fragment velocity*

<b>Target material</b>	<b>Total target thickness (mm)</b>	<b>Average fragment velocity</b>	<b>Standard deviation of fragment velocity</b>
Al 5083	13	2232	1496
	44.5	2365	1563
	89	2692	1451
	133.5	3115	1649
RHA	1.6	1710	939
	6	1653	962
	12	1681	978
	18	1682	951
	25.5	1698	978
	51	1811	960
	127.5	2117	1017

Figure 11 shows the normalised velocity distributions for all material thicknesses tested. The numbers are shown as percentage of the sum of all fragments collected for each material. 90% of steel fragments are below 3500 m/s. In comparison, 90% of the aluminium fragments are below 4500 m/s. This larger relative velocity spread can be explained by the fact that the aluminium fragments, having a lower mass for the same volume, need a higher velocity to penetrate the witness sheets.

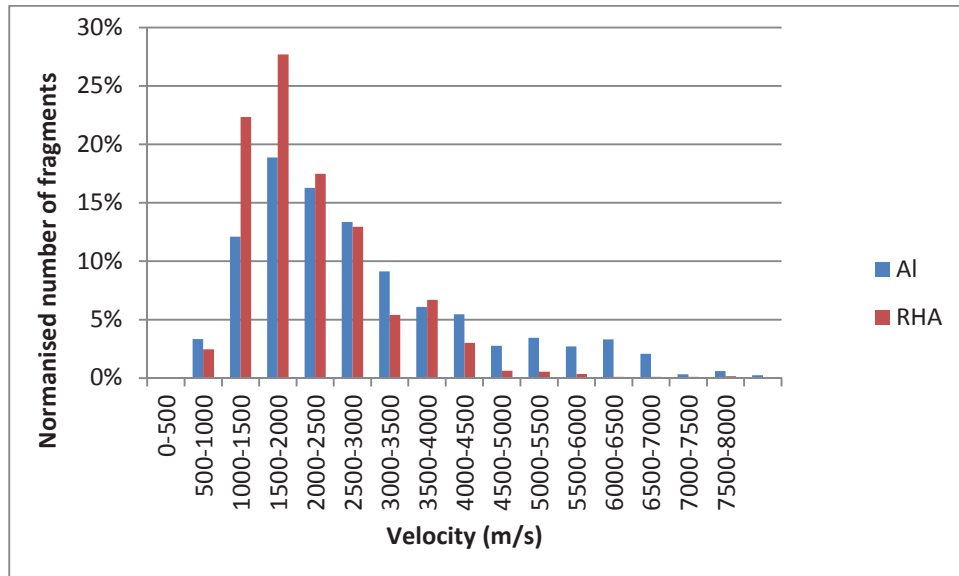


Figure 11: Normalised velocity distributions for all thicknesses tested

#### 4.2.5 Discussion on high velocities

As shown in Subsection 4.2.4, witness pack analysis yields a low number of fragments with velocities higher than 1000 m/s when using the THOR penetration model in DeCaM.

Such high velocities were not found with the previous model used in DeCaM, which estimated velocities based on the Velocity Threshold Curves (VTC). VTC were limited to lower velocities (usually below 1000 m/s) and were not accurate for very small fragment masses, like the ones produced by shaped charge impacts.

In order to validate these findings, a high speed camera was used to film a behind armour debris cloud during one of the tests performed on 25.5 mm RHA, to verify the existence of those very fast fragments. The camera recorded at a frame rate of 40 000 frames/second. Still images were taken of two frames. Fragment traces can be seen and tracked from one frame to another on the outer limit of the fragment cloud. Those fragments would be amongst the fastest in the cloud viewed from the angle where the picture is taken. Figure 12 shows the two frames with fragment identification.

The time step between the two pictures is known (25  $\mu$ s), and the distance travelled by the fragments during that time can be measured on the picture. With those two values, the velocity can be calculated. Table 4 shows the velocities.

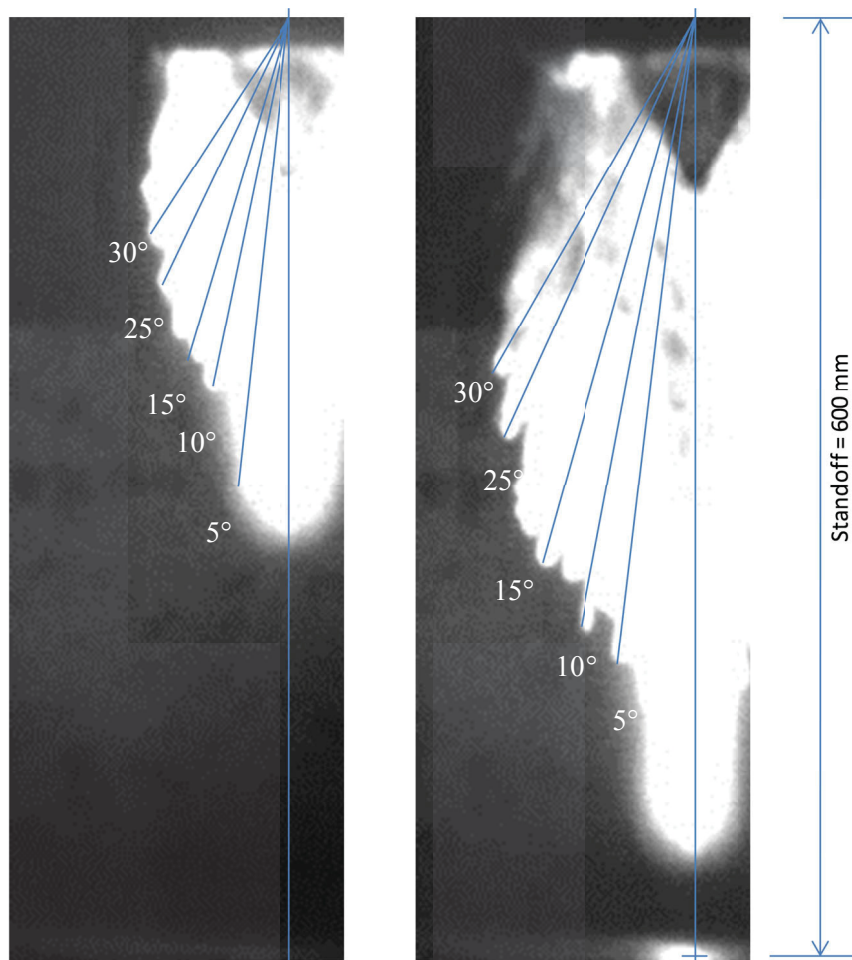


Figure 12: Behind armour debris cloud for velocity measurements

Table 4: Fragment velocities measured on X-ray

Azimuth angle (°)	Velocity measured on X-ray (m/s)
0° (jet tip)	8320
10	6200
15	5520
25	4000
30	3640

Figure 13 shows the velocities versus azimuth angle measured on the high speed film along with the velocities versus azimuth angle calculated using the THOR model in DeCaM for the three shots with the same target thickness and material (25.5 mm RHA) as the high speed film.

As visible in Figure 13, there are fragments with velocities above those measured on the high speed film. They can be explained. Firstly, the high speed film data is from only one shot and one angle of view. It is possible that faster fragments occurred during the other two shots shown on the graph, or in other angles of view. Secondly, shape factors [3], like the one used for the mass and velocity calculations represent an average. This yields to a small error in the mass and velocity calculation. The third reason for the high velocities is caused by the analysis tool DeCaM: if a small hole on the first plate of the witness pack (caused by a small fragment) is close to a large hole (caused by a large fragment), it is possible that DeCaM matches the small hole on the first plate of the witness pack to the large hole on subsequent witness plates, causing the velocity calculated for this small fragment to be unrealistically high. This problem will be solved in the next version of DeCaM, but for this analysis, it was decided to remove all fragments with velocities above 8000 m/s from the analysis. This affects approximately 0.6% of the fragments. The value of 8000 m/s was chosen because it is the approximate jet tip velocity for this size of shaped charge.

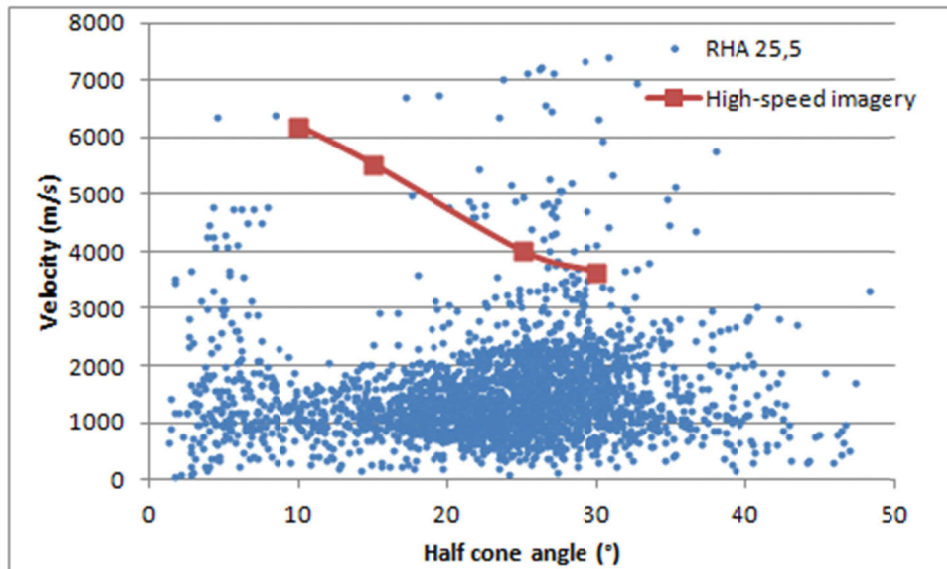


Figure 13: Velocity measurements (pictures and from WPAS) versus azimuth angle

### 4.3 Fragment spatial distribution

As seen in Figure 12, the behind armour debris from shaped charge impacts are most often characterised by a cone whose apex is the point on the target where the shaped charge jet exited the plate. This is also illustrated in Figure 14. The distribution of debris in this cone can be described with conical zones behind the target; each zone being defined by two cones with slightly different openings (say  $d\theta = 5 - 10^\circ$ ).

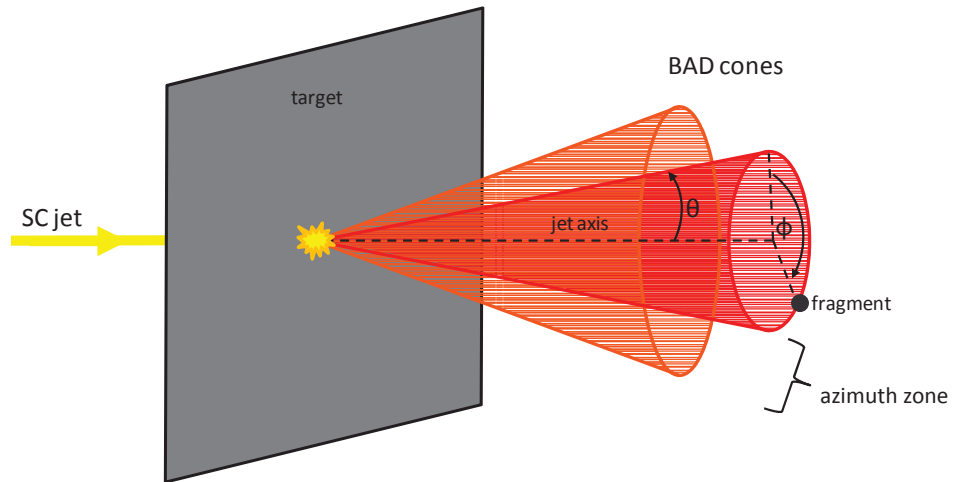


Figure 14: Geometry of BAD cones

Figures 15 and 16 show the fragment spatial distributions for aluminium and steel with respect to the azimuth angle (also called half-cone angle).

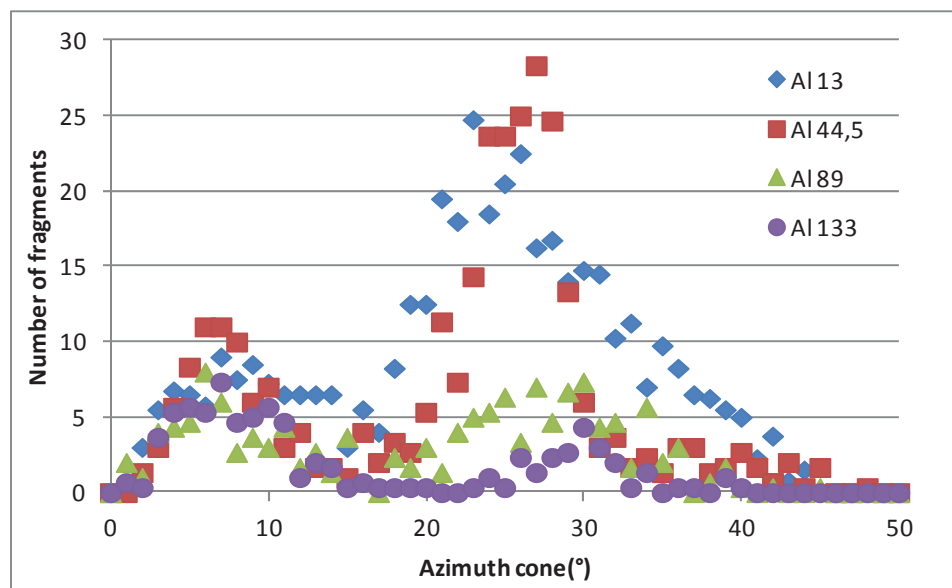


Figure 15: Experimental distribution of the BAD versus azimuth angle for Al ( $d\theta = 1^\circ$ )

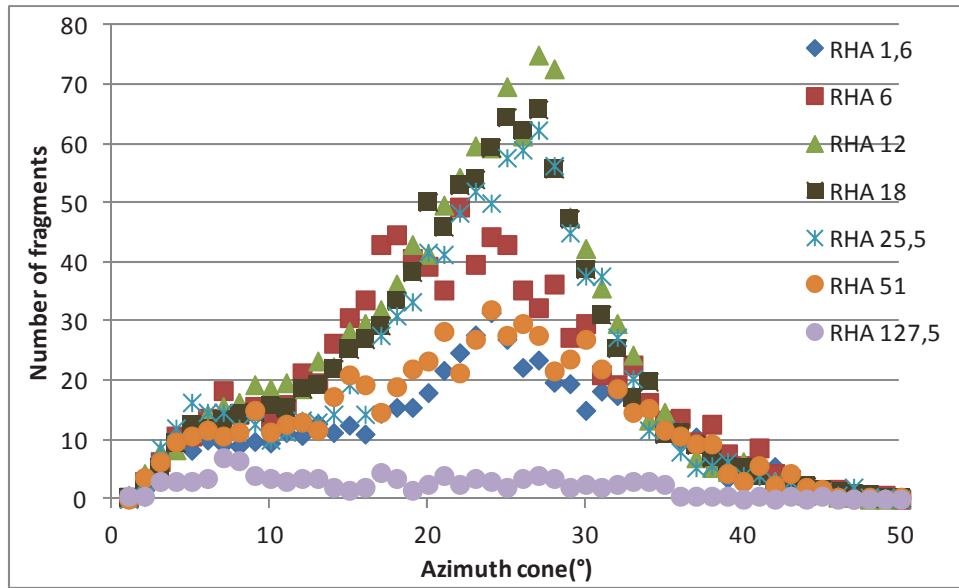


Figure 16: Experimental distribution of the BAD versus azimuth for RHA ( $d\theta = 1^\circ$ )

The number of fragments versus azimuth can be characterised by a bimodal (2-peak) Gaussian distribution that starts at  $0^\circ$  (jet axis). Subsection 5.1.4 includes an additional discussion on the spatial distribution Probability Distribution Function.

The presence of two modes in Figures 15 and 16 may be explained with some features in Figure 12. A high speed cloud of fragments seems to closely follow the jet of the shaped charge. This cloud could be formed by drops from the shaped charge jet along with some plate debris. They would essentially move on the jet axis but with some radial dispersion. The left slope of the first peak observed in Figures 15 and 16 might have been different if all single fragment holes would not have merged to create a large single one. The second peak would be the result of spallation at the back of the plate (small cone behind the plate in Figure 12) releasing much slower fragments. This explanation would explain the relative importance of the two peaks as well as their evolution, but would still require further confirmation.

## 4.4 Fragment lethality

### 4.4.1 Calculation of the Percentage of Incapacitation (PI)

Calculation of the PI is based on occupants positioned as shown in Figure 17 with respect to the impact point. The closer the occupant is to the impact point, the more fragments have chances to impact him. The PI changes with respect to the offset distance or offset angle from the occupant to the jet entry point, as shown in Figure 17.

Figure 18 shows the side view of the zone where the fragment cone impacts the occupant (exposed surface area).

The PI is calculated for occupants sitting with their back at 60 cm standoff from the wall impacted by the shaped charge as shown in Figure 17.

The PI is calculated for offsets between 72 cm ( $50^\circ$  offset angle) where the occupant is usually completely outside the debris cone, to 0 cm ( $0^\circ$  offset angle), where the jet starts hitting the shoulder, causing 100% incapacitation.

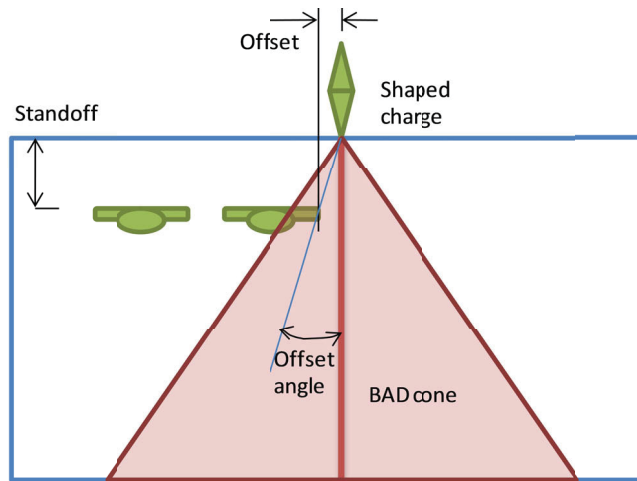


Figure 17: Schematic top view of vehicle impacted by a shaped charge

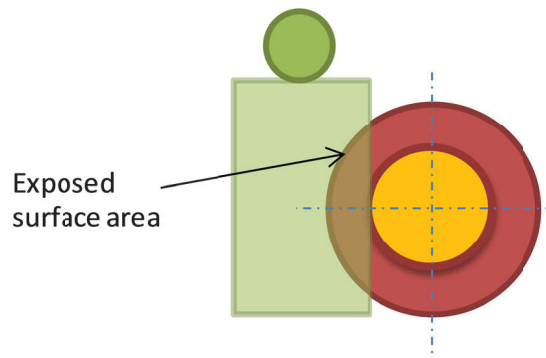


Figure 18: Side view and close-up of exposed surface area

For an occupant subjected to a cloud of debris (exposed surface area in Figure 18), the PI is calculated with the incapacitation contribution from each individual fragment in the area, as shown in the equation below.



$$PI = 1 - \prod_{i=1}^n (1 - \lambda_i) \quad (8)$$

where  $\lambda_i$  is the weighted expected level of incapacitation induced by fragment  $i$  alone, for  $i$  ranging from 1 to  $n$  fragments impacting the occupant.  $\lambda_i$  is calculated by:

$$\lambda_i = PI_i \times PHit_i \quad (9)$$

where  $PI_i$  is the level of incapacitation (PI) of fragment  $i$  calculated using Kokinakis and Sperrazza's curves [7] and  $PHit_i$  is the probability of fragment  $i$  actually hitting the target.

$PI_i$  depends on the fragment mass  $m$  (grain) and velocity  $V$  (ft/s).

$$PI_i = e^{-a \cdot (mV^{3/2} - b)^n} \quad (10)$$

Parameters  $a$ ,  $b$  and  $n$  depend on the PI criterion [7]. The PI criterion used here is the Percentage of Incapacitation Defence-30sec (PID-30 sec). This criterion refers to the capacity of personnel to accomplish a defence mission for at least 30 seconds. For this criterion,  $a = 1.68 \text{ E-3}$ ;  $b = 26500$  and  $n = 0.41356$ .

$PHit_i$  is the probability a fragment, travelling at a azimuth angle  $\theta_2$  shown in Figure 19, to impact the exposed surface area. Assuming an even distribution of the probability of occurrence of fragment  $i$  around angle  $\theta_2$ ,  $PHit_i$  is the ratio of arc  $S$  (yellow in Figure 19) to the circumference of the circle  $C$  of radius  $R_2$  (purple in Figure 19).

It is calculated by:

$$PHit_i = \frac{S}{C} = \cos^{-1} \left( \frac{\tan \theta_1}{\tan \theta_2} \right) / \pi \quad (11)$$

The parameters are shown in Figure 19. They are explained in the list below:

- Standoff = Distance between the rear target exit hole and the center of the witness pack
- $\theta_1$  = Angle between the center of the witness pack and the edge of the area covered
- $\theta_2$  = Angle between the center of the witness pack and the fragment location
- $S$  = Length of arc of a circle.
- $R_1$  = Distance between the center of the witness pack and the edge of the area covered by the occupant
- $R_2$  = Distance between center of the witness pack and the fragment location
- $C$  = Circumference of the circle of radius  $R_2$

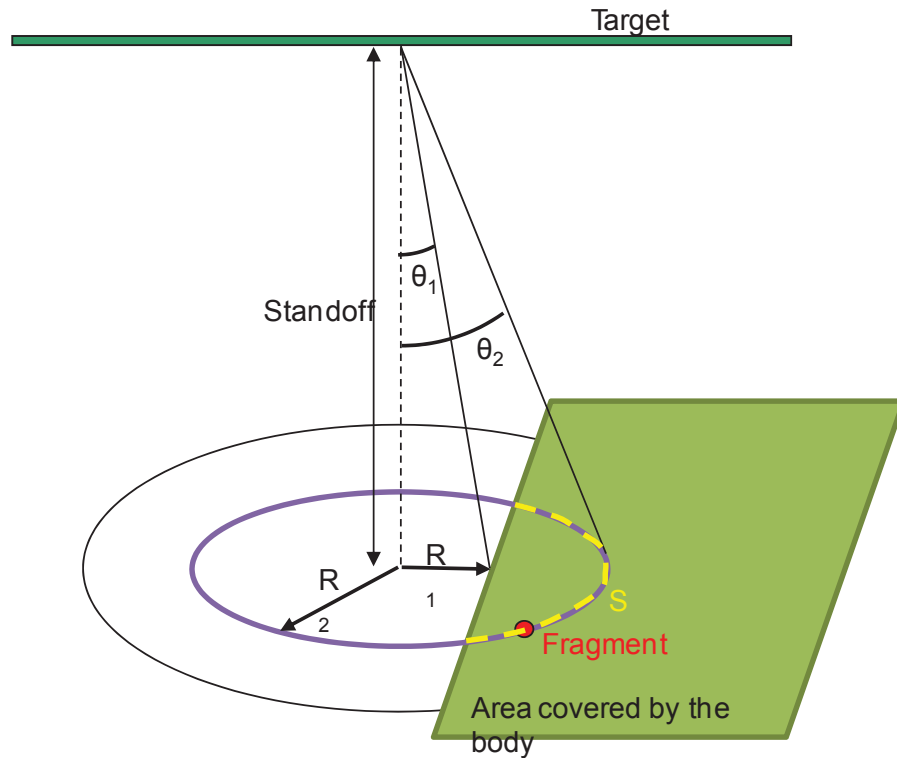


Figure 19: Area for PHit calculation

#### 4.4.2 Percentage of incapacitation results

The PIs are shown in Figure 20 for the RHA, for all thicknesses tested.

The PIs in RHA stay similar with increasing thickness (reaching 10% early in the debris cone, at approximately  $45^\circ$ , and 100% at  $30^\circ$ ) up to 51 mm. The variation of number of fragments from about 700 to about 1200 for these thicknesses has virtually no effect on the PI curves. The 127.5 mm thickness, however, shows the effect of the thickness (and consequently, the low number of fragments) on the PI, with the PI reaching 10% at  $35^\circ$  and 100% only at  $0^\circ$ . It could be considered that it may exist a critical thickness between 51 and 127.5 mm for which PI will start decreasing significantly. Additional test with targets between these thicknesses might allow identifying such a critical thickness.

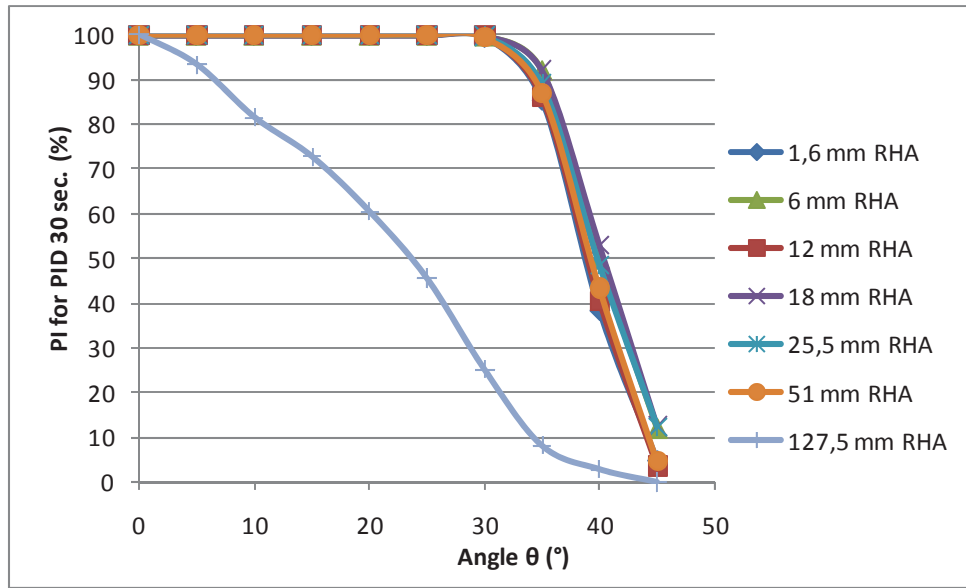


Figure 20: Percentages of incapacitation for RHA

The PIs are shown for aluminium in Figure 21, for all thicknesses tested. The PI distributions for 13 mm and 44.5 mm of aluminium are similar to the RHA distributions between 1.6 mm and 51 mm.

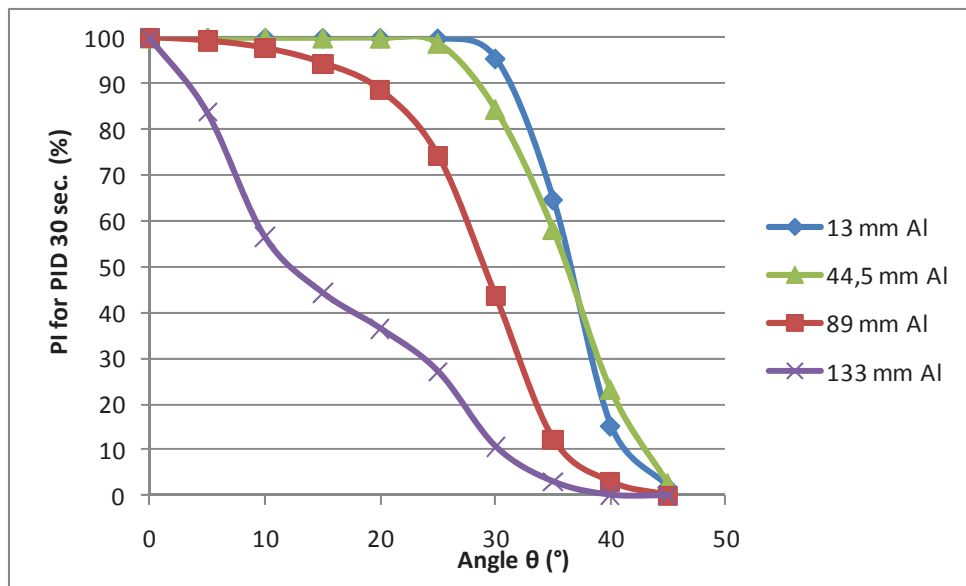


Figure 21: Percentages of incapacitation for aluminium

It can be considered that there is a critical thickness, or number of fragments for which the fragment PI starts to drop. Tests on in-between thicknesses might have shown the turning point where the effect of thickness (or lower number of fragments) starts affecting the PI.

To better illustrate the difference between the materials, the PIs are compared for similar thicknesses, and areal densities (Figure 22).

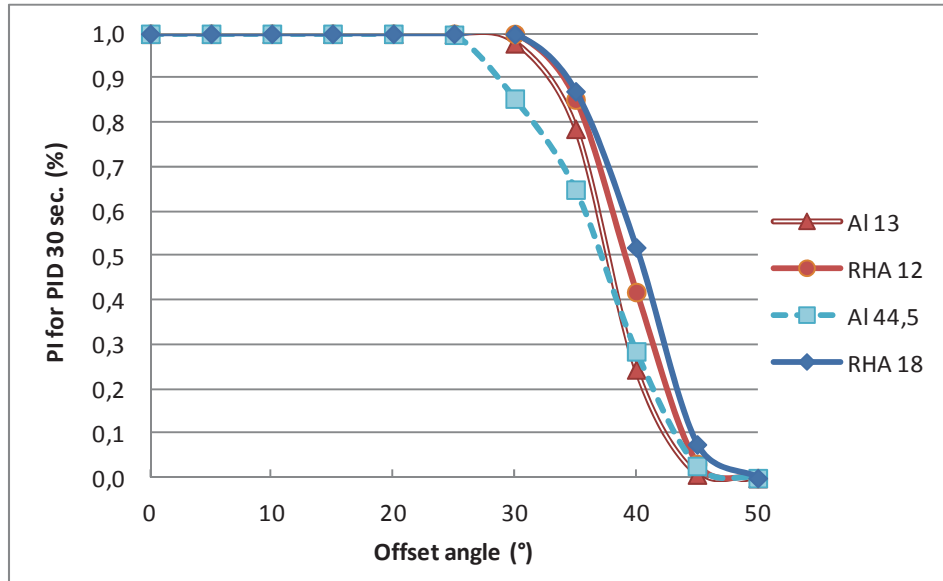


Figure 22: PI for 13 mm Al, 12 mm RHA and 44.5 mm aluminium

For similar thicknesses (13 mm for aluminium, 12 mm for RHA), although the average number of fragments was approximately three times lower for the aluminium targets (408 fragments) than for the RHA targets (1165), the PI distributions are similar for both materials, whilst slightly lower for aluminium. For example, the PI reaches 10% at approximately 44° for RHA versus 42° for aluminium.

To compare similar densities, Figure 22 also shows the PI data for 44.5 mm of aluminium. This corresponds to  $118 \text{ kg/m}^2$ . This areal density is between 12 mm steel ( $94 \text{ kg/m}^2$ ) and 18 mm steel ( $141 \text{ kg/m}^2$ ), also shown in Figure 22. Again, the distributions are similar for both materials, with still aluminium being slightly lower than RHA. This time, the difference is larger, with PIDs approximately 0.18 less for aluminium than RHA. Looking at Figures 17 and 18, it can be deduced that this tendency will continue to increase up to  $355 \text{ kg/m}^3$  (133.5 mm aluminium).

This page intentionally left blank.

## 5 Data consolidation into a vulnerability model

---

Further calculations involving more complex scenarios and target geometries could be performed with the in-house V/L tool Survivability and Lethality Assessment and Modelling Software (SLAMS) [9]. SLAMS allows to simulate attacks with various types of threats (chemical and kinetic) against targets with different possible levels of complexity, from a simple box to a complete CAD model with logical systems.

No matter what kind of target is involved, the treatment of BAD, or any other source of fragments, requires the user to provide some specific information about the fragment cloud produced by the concerned threat. Most of this information is probabilistic in nature and must be inputted as distributions. This annex proposes a method for consolidating the experimental data presented in this report into BAD models in relation with the shaped charge and metallic plate combinations. It is based on mass, energy and azimuth distributions; the fragment table will be generated by cumulating fragment patterns built randomly from these distributions while ensuring conservation of mass and energy. In order to build a versatile model not limited to setups used in the trials, experimental data was parameterized. No predictive model exists for most of the observations below, so the empirical fits were done with some arbitrary function yielding satisfying results. They are not to be interpreted as the validation of some physics-based model.

### 5.1 Data parameterization

The first step is to parameterize the data with distribution functions. The cumulative mass and energy distributions were both first fitted for each material and thickness with a generic curve, the latter being defined by parameters. The resulting sets of these parameters were afterward fitted as a function of the thickness for each material.

#### 5.1.1 Cumulative mass distribution

The predicted cumulative mass distribution<sup>1</sup> of the fragments is:

$$n_m^\Sigma = \frac{m^a}{b^a + m^a} \quad (12)$$

where  $m$  is the mass of the fragment (g) and where  $a$  (non-dimensional) and  $b$  (g) are fit parameters. The values for these parameters are given as a function of the thickness  $T$  (mm).

---

<sup>1</sup> *i.e.* the proportion of fragments with a mass less or equal to some mass value.

For RHA they are:

$$\begin{aligned} a &= 1.02131 \\ b &= \begin{cases} 0.01633 + 3.52212 \times 10^{-4}T & T \leq 12 \\ 0.0235 e^{-T/82.9954} & T > 12 \end{cases} \end{aligned} \quad (13)$$

For aluminium, they are:

$$\begin{aligned} a &= 0.8729 \\ b &= 0.01402 e^{-T/83.84487} \end{aligned} \quad (14)$$

Figures 23 and 24 present the experimental and predicted cumulative mass distribution for RHA targets with thicknesses of 1.6 mm, 12 mm, 25.5 mm and 127.5 mm while those for Al targets (13 mm, 44.5 mm, 89 mm, 133 mm) are presented in Figures 25 and 26.

### 5.1.2 Cumulative energy distribution

In the case of the fragment energy, the cumulative distribution is given by:

$$n_{\varepsilon}^{\Sigma} = \frac{\varepsilon^c}{d^c + \varepsilon^c} \quad (15)$$

where  $\varepsilon$  is the single-fragment energy  $\varepsilon = mv^2/2$  (J) and where  $c$  (non-dimensional) and  $d$  (J) are parameters fitted as a function of the thickness  $T$  (mm).

For RHA they are:

$$\begin{aligned} c &= 1.50018 + 0.0086T \\ d &= 0.57875 + 17.32354 \cdot 0.99395^T \end{aligned} \quad (16)$$

For aluminium, they are:

$$\begin{aligned} c &= 2.06462 + 0.00274T \\ d &= 8.68102 + 11.09084 \cdot 0.99094^T \end{aligned} \quad (17)$$

These functions are presented along with experimental distributions in Figures 27 to 30. One may notice in these figures a gap sometimes appears between the smooth behaviour of the analytical function and the almost saturated experimental distribution. This feature means the energy distribution (and therefore the velocity distribution since the mass distributions do not exhibit this irregularity) is bimodal. This bimodality could be observed in Figures 9 and 10. More could be found in Subsection 5.1.4 on the probable origin of these two populations.

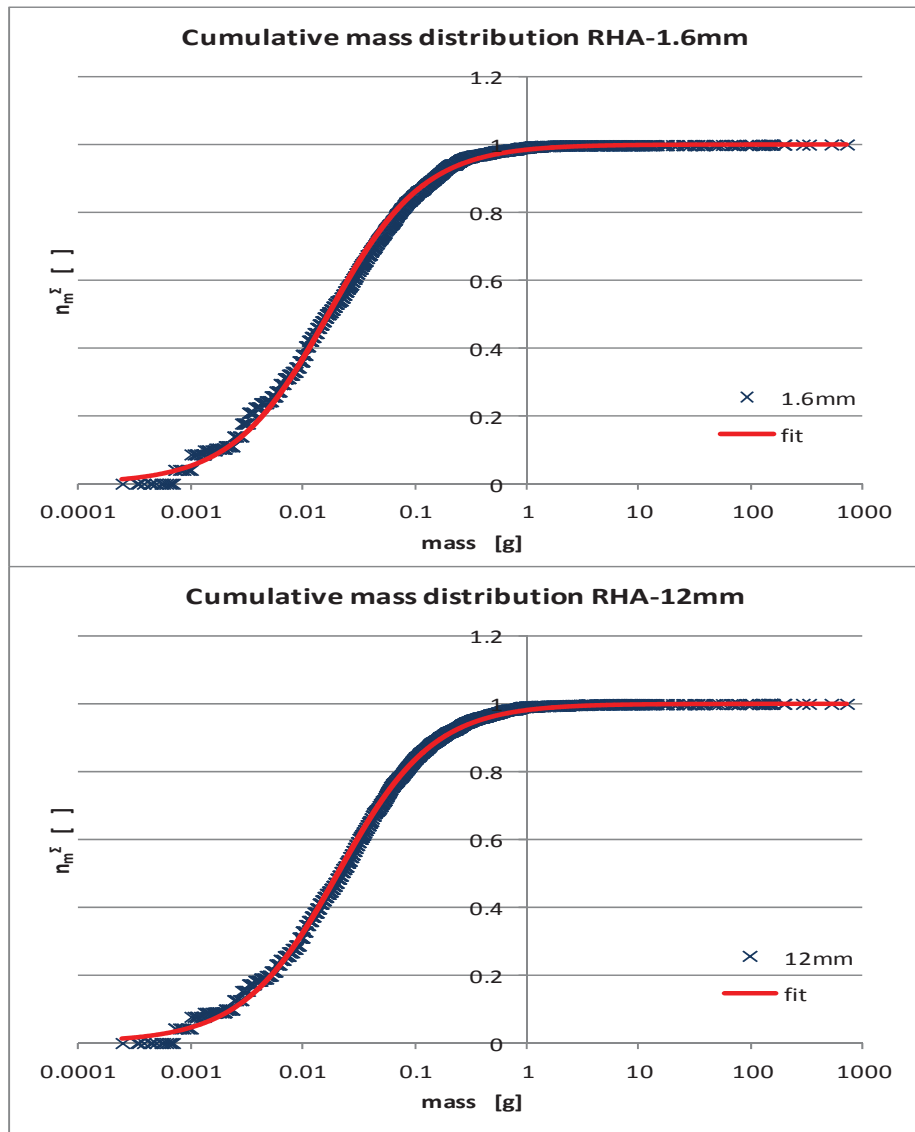


Figure 23: Experimental cumulative mass distributions of BAD for RHA plates 1.6 mm and 12 mm thick along with fit from equations 12 and 13



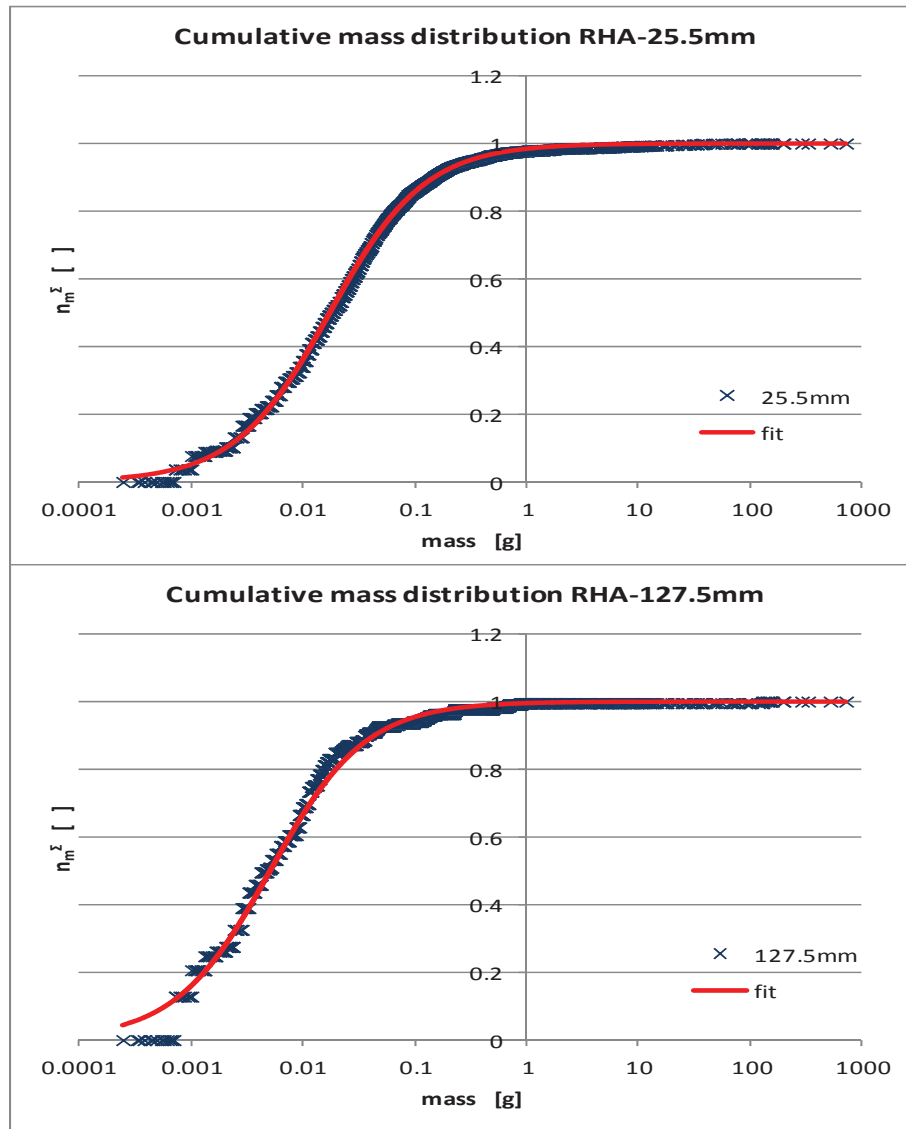


Figure 24: Experimental cumulative mass distributions of BAD for RHA plates 25.5 mm and 127.5 mm thick along with fit from equations 12 and 13

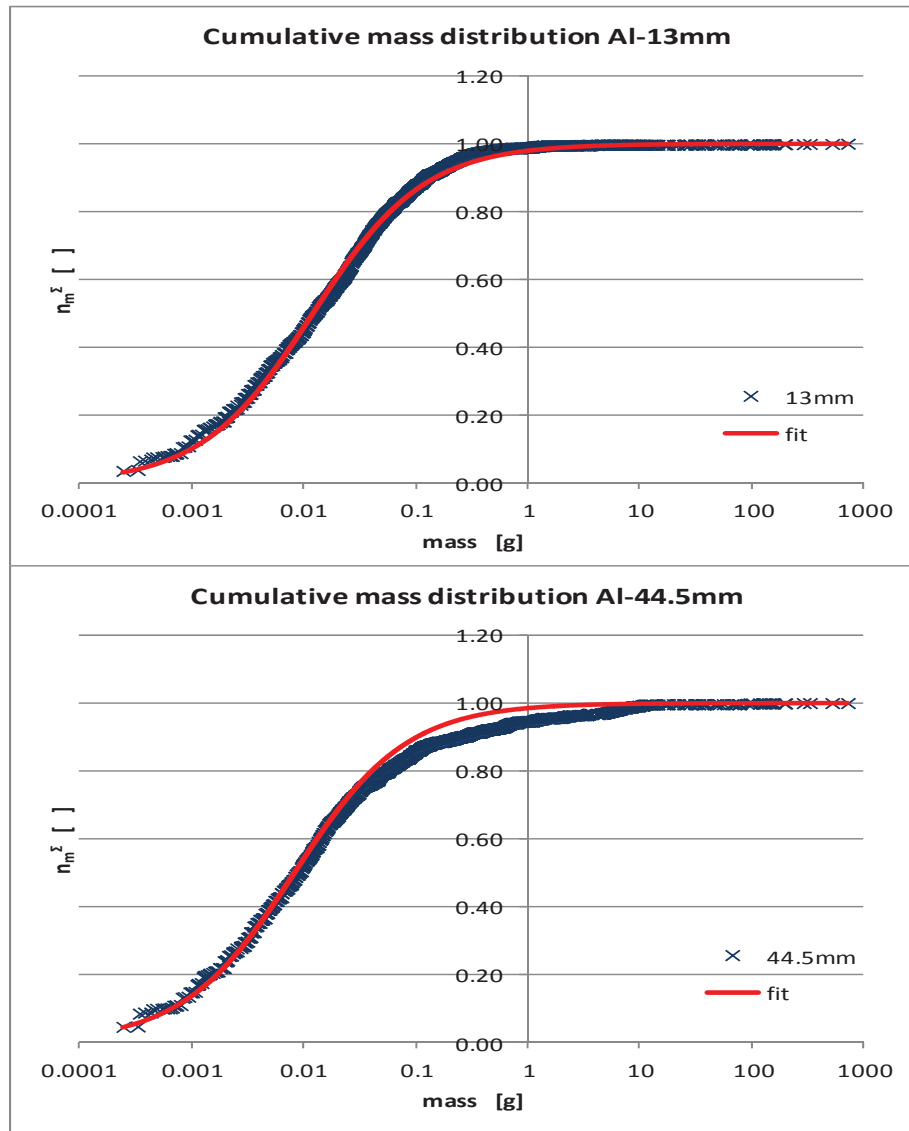


Figure 25: Experimental cumulative mass distributions of BAD for Al plates 13 mm and 44.5 mm thick along with fit from equations 12 and 14

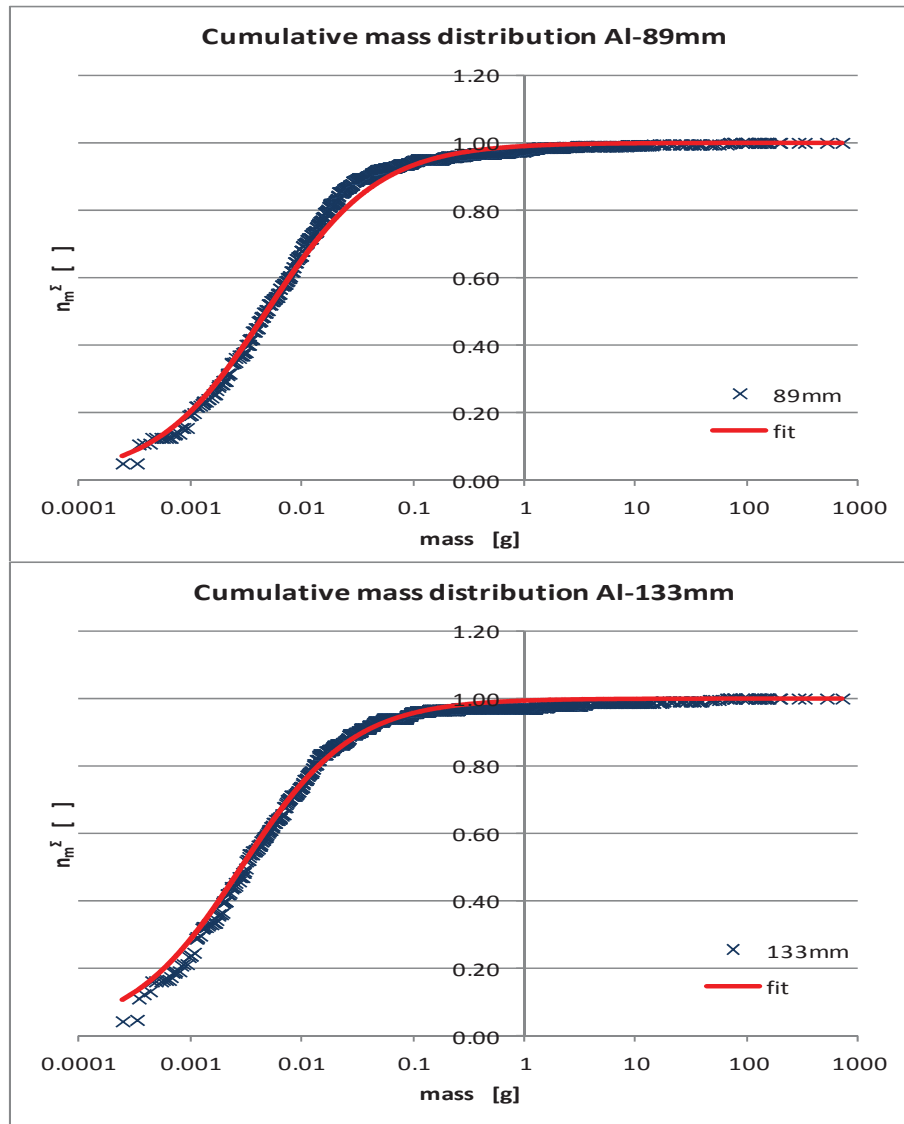


Figure 26: Experimental cumulative mass distributions of BAD for Al plates 89 mm and 133 mm thick along with fit from equations 12 and 14

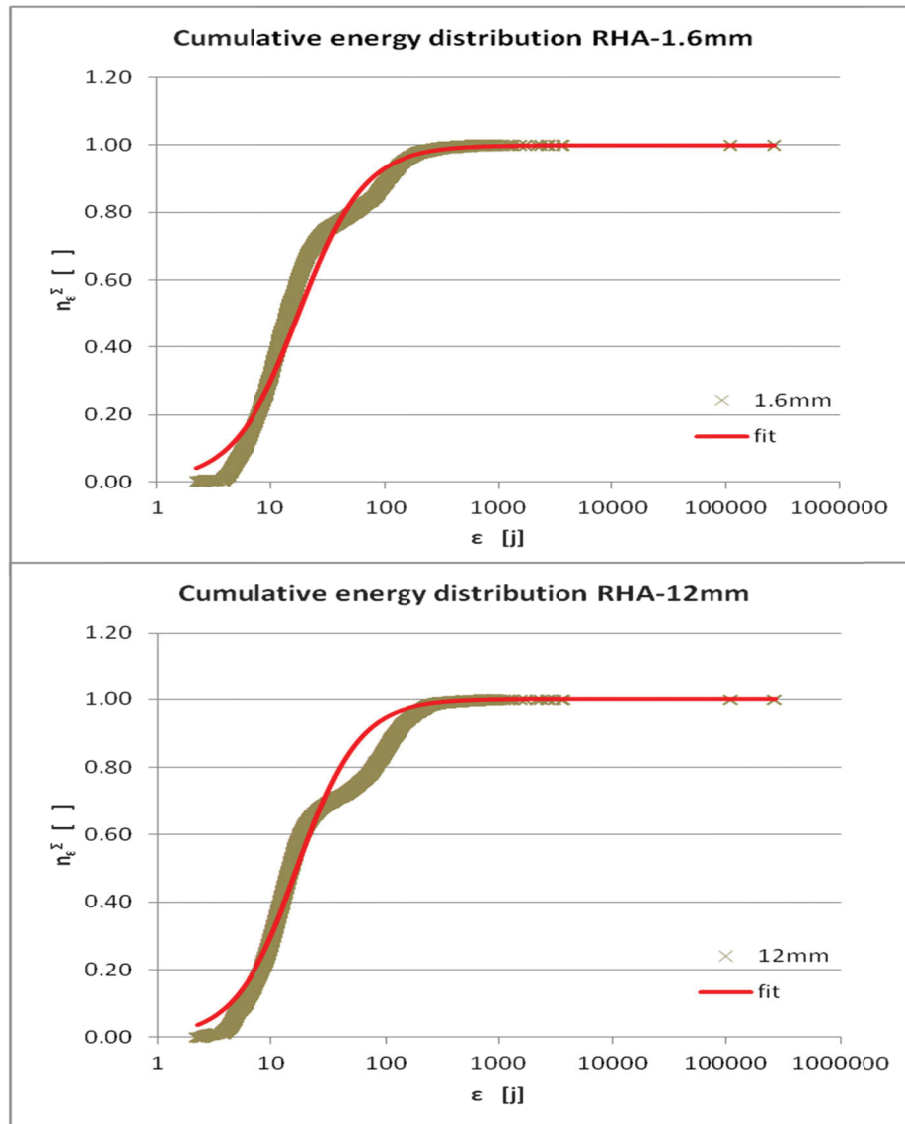


Figure 27: Experimental cumulative energy distributions of BAD for RHA plates 1.6 mm and 12 mm thick along with fit from equations 15 and 16

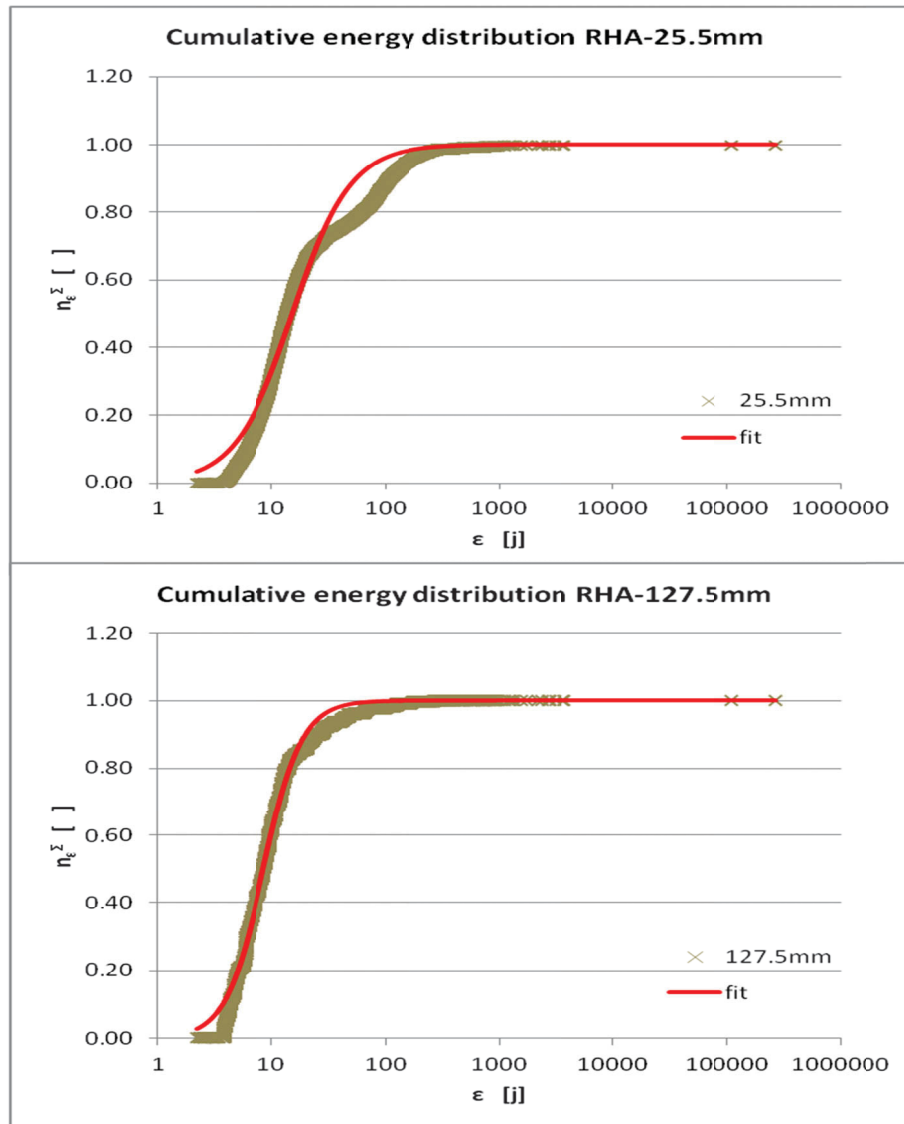


Figure 28: Experimental cumulative energy distributions of BAD for RHA plates 25.5 mm and 127.5 mm thick along with fit from equations 15 and 16

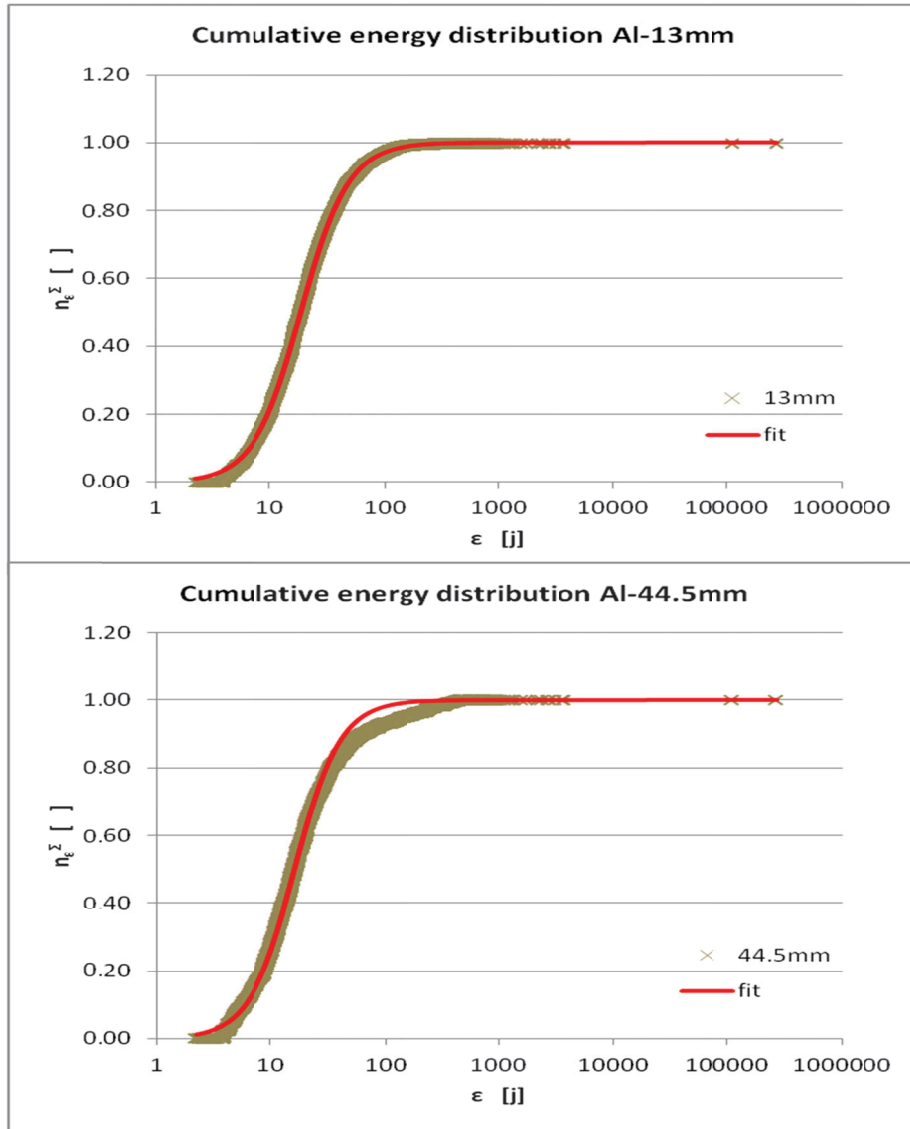


Figure 29: Experimental cumulative energy distributions of BAD for Al plates 13 mm and 44.5 mm thick along with fit from equations 15 and 17

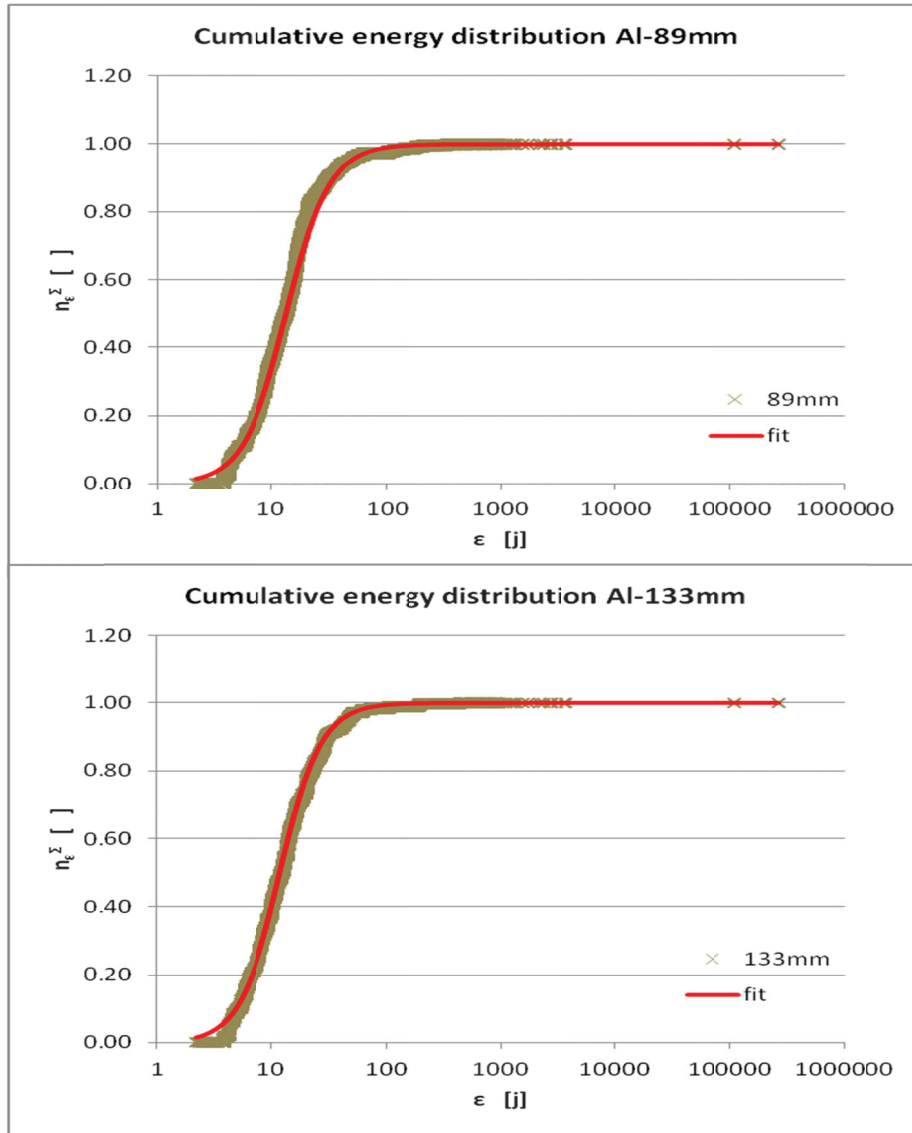


Figure 30: Experimental cumulative energy distributions of BAD for Al plates 89 mm and 133 mm thick along with fit from equations 15 and 17

The kinetic energy distribution is interesting as it carries the velocity information:

$$v_i = \sqrt{\frac{2\varepsilon_i}{m_i}} \quad (18)$$

Indeed the velocity distribution could be used directly to attribute velocities to fragments, however the energy correlates the mass and the velocity and is a quantity that must be conserved. Proceeding with energy instead of velocity will reduce arbitrariness in the velocity attribution process as all generated events will have to conserve the total energy and total mass of fragments.

These two conserved quantities were calculated and averaged over the number of trials done for each setup presented in Table 1. Since a value for both of these observations will be required during the generation of the fragment table, the curves  $E$  vs  $T$  and  $M$  vs  $T$  were parameterized.

### 5.1.3 Expected total mass and energy

The points for the expected total mass  $M$  (g) as a function of the target thickness are plotted in Figures 31 and 32 according to:

$$M = g \left[ \frac{1}{1 + e^{-(T-k)/h_1}} \right] \left[ 1 - \frac{1}{1 + e^{-(T-k)/h_2}} \right] \quad (19)$$

RHA the parameters are:

$$\begin{aligned} g &= 940 \text{ (g)} \\ h_1 &= 9.65 \text{ (mm)} \\ h_2 &= 17.5 \text{ (mm)} \\ k &= 25.5 \text{ (mm)} \end{aligned} \quad (20)$$

For aluminium, they are:

$$\begin{aligned} g &= 480 \text{ (g)} \\ h_1 &= 10.76 \text{ (mm)} \\ h_2 &= 12.81 \text{ (mm)} \\ k &= 44.5 \text{ (mm)} \end{aligned} \quad (21)$$

Equations for the expected total energy (J) are plotted in Figure 31 and 32 according to:

$$E = Q \left[ \frac{1}{1 + e^{-(T-R)/s_1}} \right] \left[ 1 - \frac{1}{1 + e^{-(T-R)/s_2}} \right] \quad (22)$$

For RHA, the parameters in equation 22 are:

$$\begin{aligned} Q &= 110\,000 \text{ (J)} \\ s_1 &= 4.4 \text{ (mm)} \\ s_2 &= 29.3 \text{ (mm)} \\ R &= 4.2 \text{ (mm)} \end{aligned} \quad (23)$$



For aluminium, they are:

$$\begin{aligned} Q &= 40\,000 \text{ (J)} \\ s_1 &= 36.2 \text{ (mm)} \\ s_2 &= 17.7 \text{ (mm)} \\ R &= 44.5 \text{ (mm)} \end{aligned} \quad (24)$$

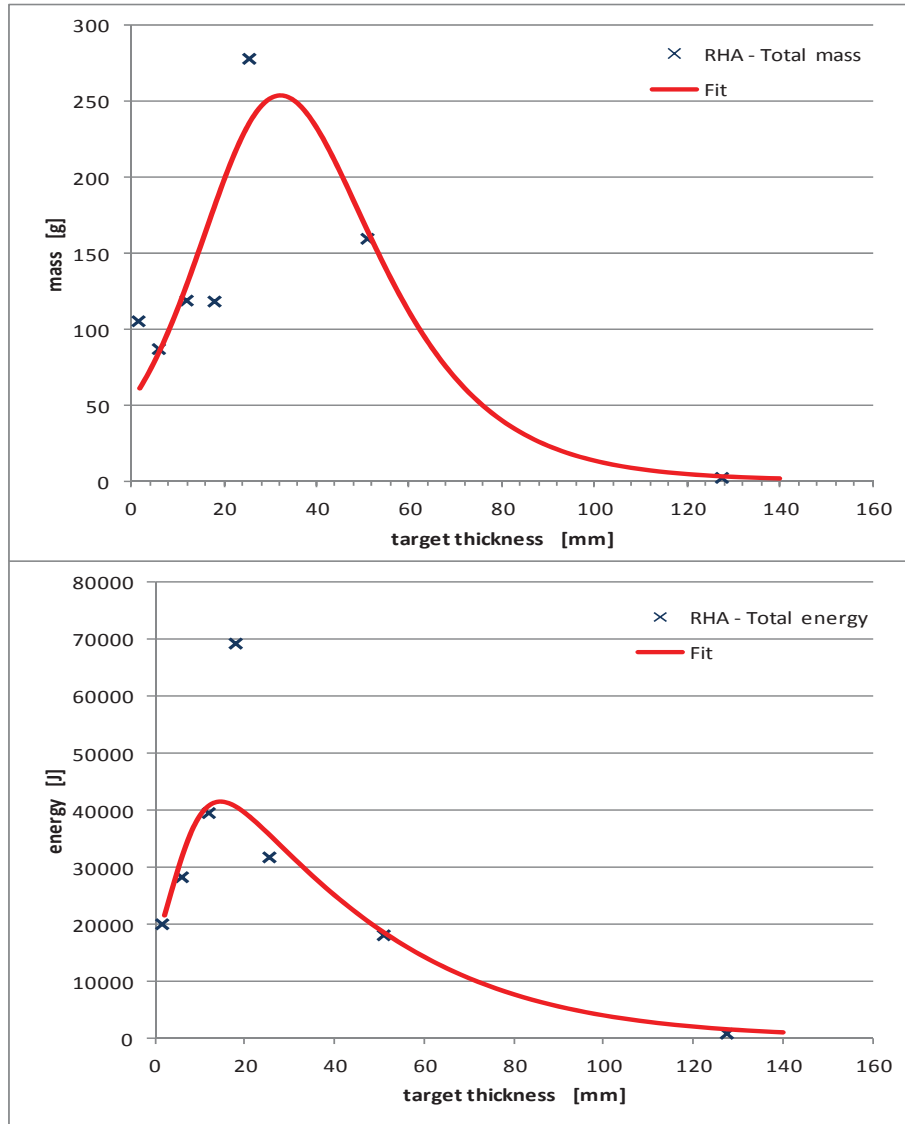


Figure 31: Expected total mass (top) and total energy (bottom) of fragments as a function of the target thickness  $T$  for RHA with fits from equations 19, 20, 22 and 23

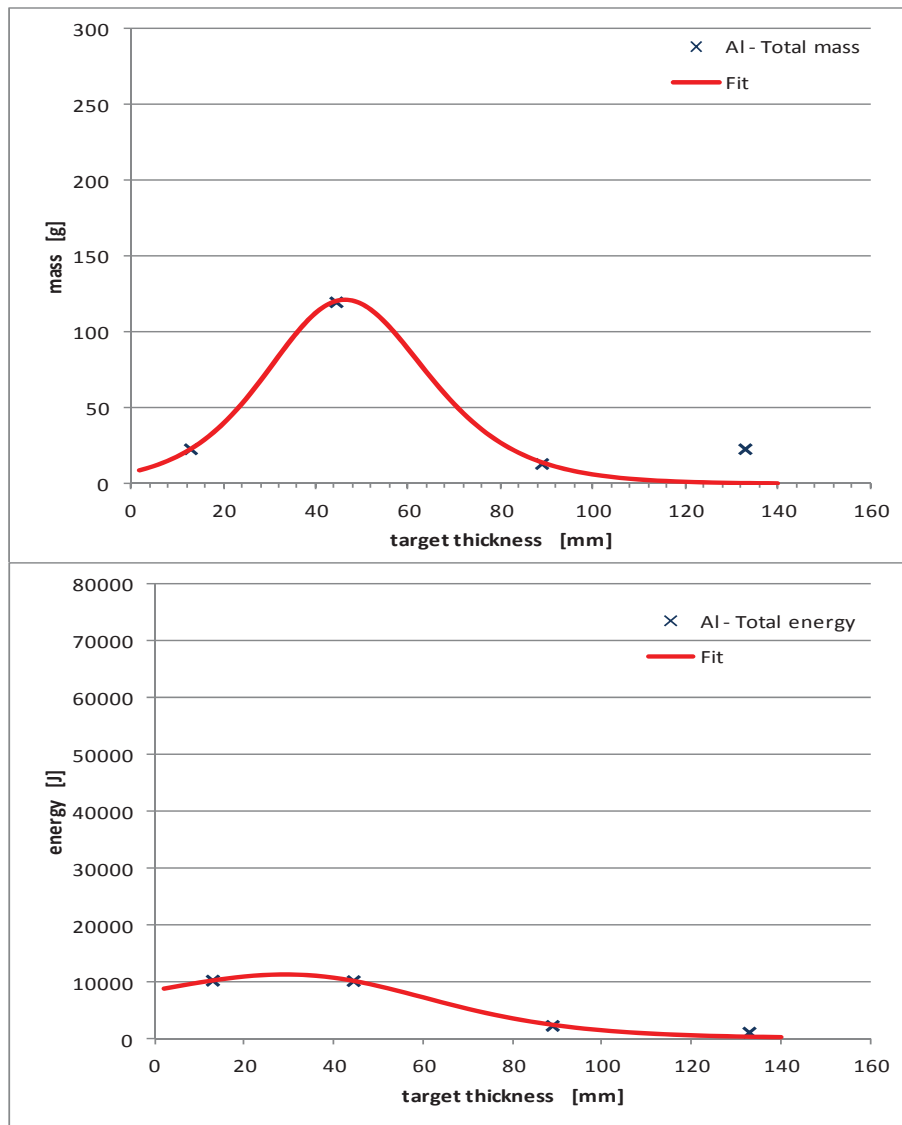


Figure 32: Expected total mass (top) and total energy (bottom) of fragments as a function of the target thickness  $T$  for Al with fits from equations 19, 21, 22 and 24

Each single data point in Figures 31 and 32 is the sum of weighted energies and masses of experimental distributions presented in Figures 23 to 30. This means they are very sensitive to the tail of these experimental distributions that features important masses or energies. Even though very high energies and masses are very unlikely with respect to light and/or slower fragments, the contributions of very massive/energetic fragments inexorably introduce an important input in the total mass and energy of fragments depicted in Figures 31 and 32. Since most massive and highly energetic pieces are usually found along the path of the remnant of the jet, it appears logical to remove these fragments from the distributions with a cut-off cone angle<sup>2</sup> ( $\theta_{cut}$ ). The value selected for  $\theta_{cut}$  is 5°. This kind of cut-off is very straightforward and requires some caution. This threshold was chosen such that the contributions from the jet that appeared excessive in terms of mass and energy were retrieved from the distributions. This threshold was also chosen such that the cloud of fragments was not too amputated and that the resulting distributions showed not too sensitive to small variations of this cut-off value. This means previous distribution in Figures 23 to 30 were subject to this cut-off value but it had no significant impact since only marginal contributions in the tail were removed. The experimental results in Figures 31 and 32 are plotted along with their fitting curves. The choice of this type of function appeared satisfactory although some discrepancies sometimes appear between experimental data and theoretical predictions (fit), but one has to keep in mind that experimental results cannot be totally cleared of any sensitivity regarding the  $\theta_{cut}$  value and that other values (or even methods) could reshape the experimental curves. Some marginal points could then end up closer to theoretical curve. Using another function could also lead to better agreements. The choice of the function was arbitrary since there is actually no physics-based model that predicts the total mass and energy of the cloud of debris. Section 5.3 proposes some solutions to improve this situation.

As a last remark, the number of fragments  $N$  produced in trials is also probabilistic by nature. In principle the total number of fragments produced from a trial to another should also follow some distribution. It is however much simpler to use a single value as predicted by equations 1 and 2 that provide the expected number of fragments for a specific setup. Still, one has to keep in mind that even this quantity carries an underlying distribution.

#### 5.1.4 Fragment spatial distribution

The last unknown is the spatial distribution of the fragments. Normalised experimental results for this Probability Distribution Function (PDF) are shown in Figure 33. As discussed in Section 4.3; the number of fragments can be characterised as a bimodal PDF.

---

<sup>2</sup> Including high values originating from the jet would introduce a bias in the mass and energy distributions because predicted fragments would on average be heavier and faster than what is actually observed experimentally.

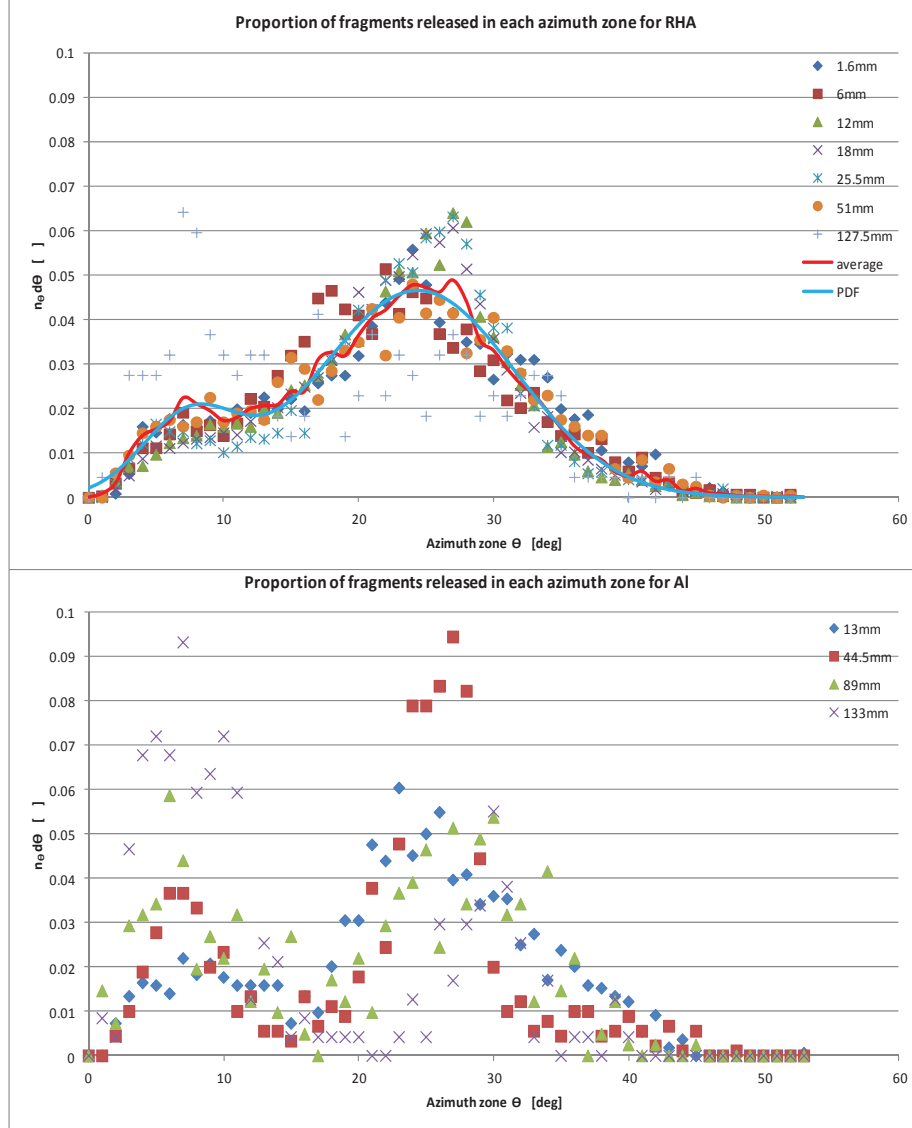


Figure 33: Experimental distribution of the BAD as a function of the azimuth opening for RHA (top) and Al (bottom)

This PDF was parameterized with a function made of two Gaussian curves:

$$n_\theta d\theta = \frac{1}{\sqrt{2\pi}(A_1\omega_1 + A_2\omega_2)} [A_1 e^{-(\theta-\theta_1)^2/2\omega_1^2} + A_2 e^{-(\theta-\theta_2)^2/2\omega_2^2}] d\theta \quad (25)$$

where  $d\theta$  is the domain volume centered at  $\theta$  that contains the proportion of fragments  $n_\theta d\theta$ .  $A_1, A_2, \theta_1, \theta_2, \omega_1$  and  $\omega_2$  are parameters that were adjusted to fit data for RHA and aluminium. It may be noticed that this PDF is much less sensitive to the thickness of the plate target in the case of RHA than it is for Al. A clear evolution from 13 mm to 133 mm is visible for Al plates (lateral

ejections increases with increasing thickness up to some optimal one before decaying for thicker targets) while this evolution may also exist for RHA but is not quite obvious; only the thickest plate (127.5 mm) shows a slightly different profile. The two modes are also not as resolved for RHA as they are for Al. It was therefore decided to fit equation 18 over each Al curve from Figure 33 but to fit only the averaged experimental curves for RHA<sup>3</sup>. In the latter case, results will be reliable but should be used with more caution for thick targets.

The best-fit parameters of equation 25 for RHA, are then:

$$\begin{aligned}
 A_1 &= 0.01718 \quad (\text{non dimensional}) \\
 A_2 &= 0.04566 \quad (\text{non dimensional}) \\
 \theta_1 &= 7.46047 \quad (\text{deg}) \\
 \theta_2 &= 24.39558 \quad (\text{deg}) \\
 \omega_1 &= 3.53395 \quad (\text{deg}) \\
 \omega_2 &= 7.25109 \quad (\text{deg})
 \end{aligned} \tag{26}$$

For aluminium, these parameters are given by:

$$\begin{aligned}
 A_1 &= 0.02033 + 1.46494 \times 10^{-5} e^{T/15.10823} \quad (\text{non dimensional}) \\
 A_2 &= 0.04126 - 0.01434 e^{-0.5((T-89)/27.58948)^2} \quad (\text{non dimensional}) \\
 \theta_1 &= 6.68 \quad (\text{deg}) \\
 \theta_2 &= 26.93 \quad (\text{deg}) \\
 \omega_1 &= 3.2 \quad (\text{deg}) \\
 \omega_2 &= 4.9 \quad (\text{deg})
 \end{aligned} \tag{27}$$

As in previous equations,  $T$  stands for the plate thickness (mm). The result of these parameterizations is displayed in Figure 33 for RHA and Figures 34 and 35 for Al.

Fragments are also ejected with a given angular position within their respective cone, referred to as  $\phi$  in Figure 14. This coordinate is much more subjective since the event setup, and thus the BAD cloud, is axisymmetric. The  $\phi$  distribution is therefore considered a uniform distribution  $n_\phi d\phi = U(0.360)$  where all  $\phi$  values are equally probable. This implies as well that the net momentum over all fragments should not show any radial components. This point will be discussed in Section 5.3.

With the estimated quantities above, the next step is to describe the procedure that will merge this information into a fragment table containing all relevant and synthesized information for SLAMS.

---

<sup>3</sup> In the situation where predicted results for the 127.5 mm thick RHA target prove to deviate from the expected ones, another PDF specific to this thickness, could be defined and interpolation between this PDF and the averaged one would be used for intermediate thicknesses.

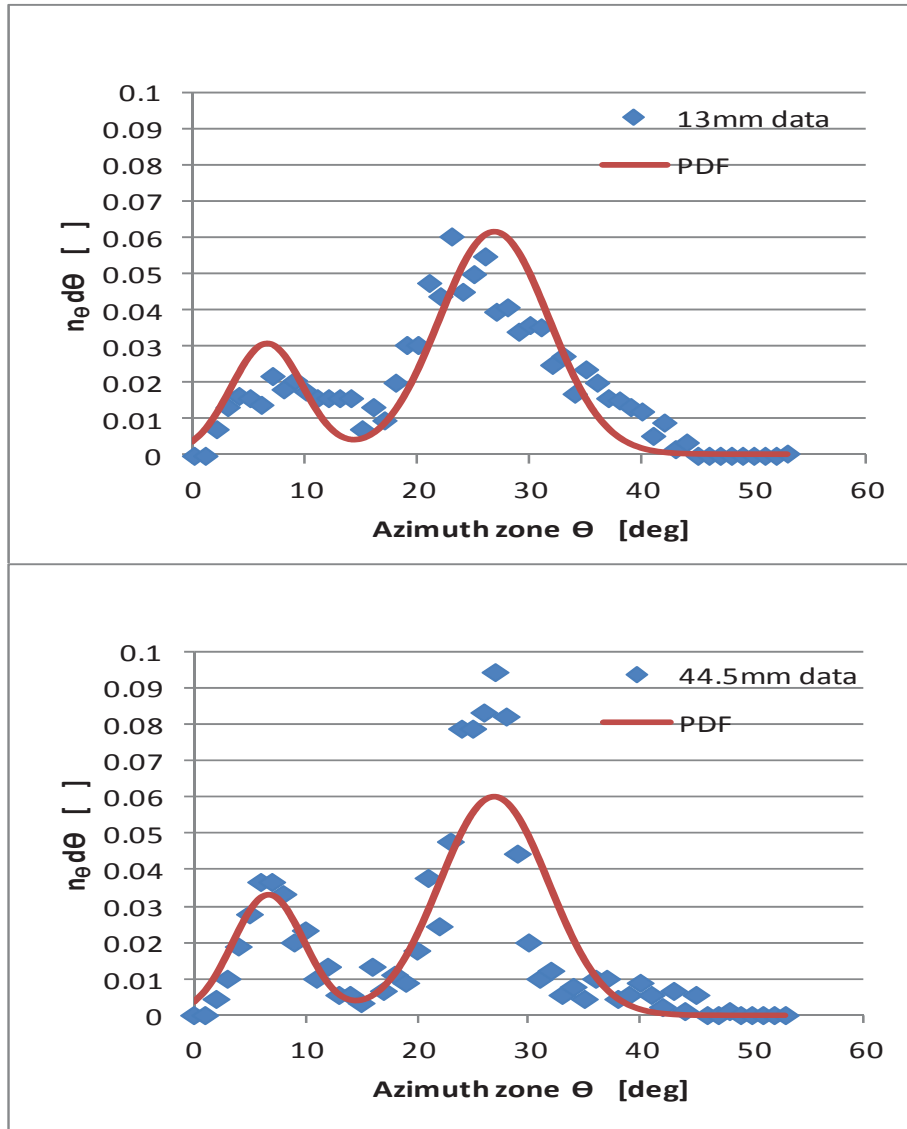


Figure 34: PDF for azimuth BAD distribution for Al plates 13 mm (top) and 44.5 mm (bottom) thick

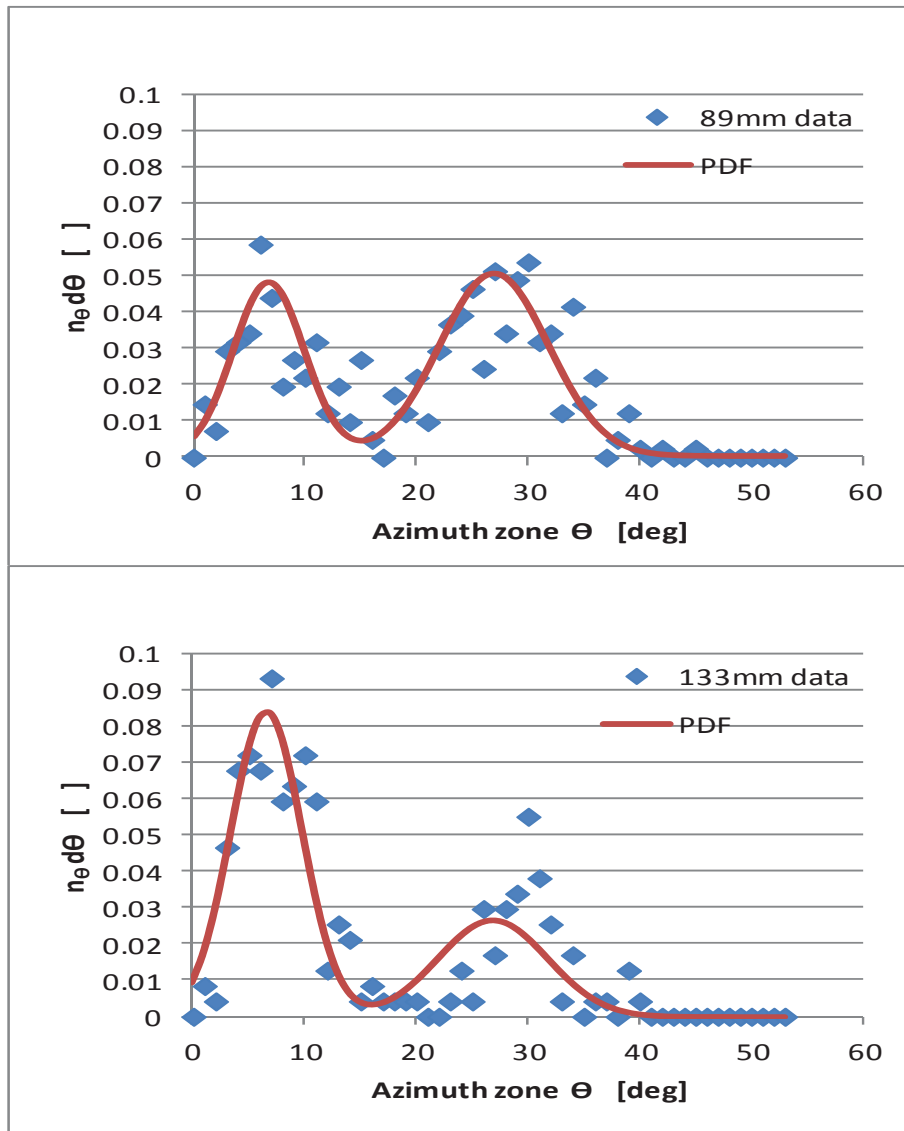


Figure 35: PDF for azimuth BAD distribution for Al plates 89 mm (top) and 133 mm (bottom) thick

## 5.2 Fragment table set up

The following algorithm could be used in two different ways: to set up a fragment table that can be used in models such as SLAMS [9] or GVAM [10, 11] (General Vulnerability Assessment Model) for further vulnerability studies or to attack a target (without explicit fragment table) in SLAMS. The latter approach is possible in SLAMS only because in its attack scenarios, it propels fragments by Monte Carlo ray tracing whereas GVAM projects fragment density onto the target which must involve a complete knowledge of the fragment pattern before running the attack scenario.

An iterative process is first used in order to get the mass of each fragment along with its energy (and incidentally their velocity) but also to ensure the conservation of these two quantities. Figure 36 represents an example of a cumulative distribution used in the algorithm and its division into sub-domains. In this example, the total value is  $X$  and  $N^x$  domains of volume  $dx$  are used to discretize the distribution. A fragment with  $x = x_i$  falls in the domain whose center is  $x_i^{\text{dom}} = \frac{5}{2}dx$ . All possible  $x_i$  in a given domain are therefore equiprobable.

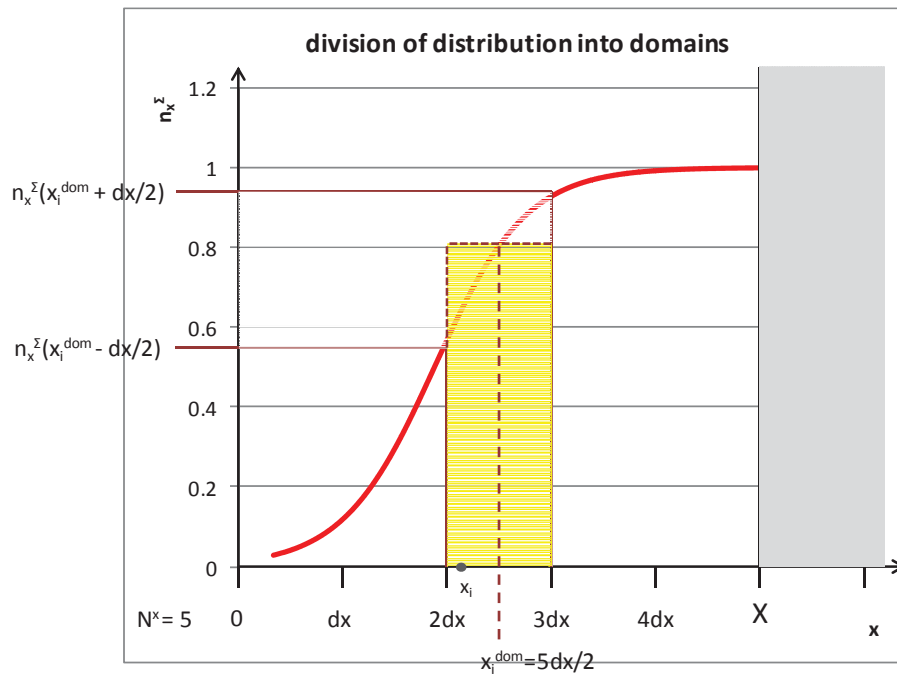


Figure 36: Illustration of domains in a distribution (e.g. cumulative) for a variable  $x$



1. Determine the expected total mass of fragment  $M$  and total energy  $E$  related to the plate thickness in the scenario with equations 19 and 22 along with the expected number of fragments  $N$  with equations 1 and 2.
2. Define the appropriate number of domains  $N^m$ ,  $N^\varepsilon$  and  $N^\theta$  in the distributions such that the obtained resolutions (domains volume)  $dm = M/N^m$ ,  $d\varepsilon = E/N^\varepsilon$  and  $d\theta = 90/N^\theta$  are realistic (see Figure 36).
3. Iterate for  $i = 1$  to  $N - 1$ , *i.e.* all fragments except the last one:
  - 3.1. Randomly pick a mass  $m_i \in ]0, M - \sum_{j=1}^{i-1} m_j [$ 
    - 3.1.1. Determine in which domain the mass  $m_i$  is in to get the center  $m_i^{dom}$  of this domain (see Figure 36)
    - 3.1.2. With equation 12 calculate  $dn = n_m^\Sigma \left( m_i^{dom} + \frac{dm}{2} \right) - n_m^\Sigma \left( m_i^{dom} - \frac{dm}{2} \right)$
    - 3.1.3. Accept mass  $m_i$  with probability  $dn$
  - 3.2. Randomly pick an energy  $\varepsilon_i \in ]0, E - \sum_{j=1}^{i-1} \varepsilon_j [$ 
    - 3.2.1. Determine in which domain the energy  $\varepsilon_i$  is in to get the center  $\varepsilon_i^{dom}$  of this domain (see Figure 36)
    - 3.2.2. With equation 15 calculate  $dn = n_\varepsilon^\Sigma \left( \varepsilon_i^{dom} + \frac{d\varepsilon}{2} \right) - n_\varepsilon^\Sigma \left( \varepsilon_i^{dom} - \frac{d\varepsilon}{2} \right)$
    - 3.2.3. Accept energy  $\varepsilon_i$  with probability  $dn$
    - 3.2.4. Compute velocity with equation 18
4. The last fragment ( $i = N$ ) gets the remaining mass  $m_N = M - \sum_{j=1}^{N-1} m_j$  and energy  $\varepsilon_N = E - \sum_{j=1}^{N-1} \varepsilon_j$

With the previous procedure, mandatorily  $N$  fragments are generated, the total mass and energy are conserved to values predicted by equations 19 and 22 and their underlying distributions obey equations 12 and 15. In this process, “acceptation” and “rejection” is done by comparing  $dn$  with a random number  $x \in ]0,1]$ . If  $x \leq dn$ , the trial state is accepted, otherwise it is rejected.

At this point the  $N$  fragments each have a mass and a velocity. The ejection angle must finally be chosen such that it respects equation 25:

5. Iterate for  $i = 1$  to  $N$ , *i.e.* all fragments:

5.1. Randomly pick an azimuth angle  $\theta_i \in [0,90]$

5.1.1. Determine in which domain the azimuth  $\theta_i$  is in to get the center  $\theta_i^{dom}$  of this domain (as in Figure 36, but with a PDF instead)

5.1.2. With equation 25 calculate  $dn = n_\theta(\theta_i^{dom}) d\theta$

5.1.3. Accept azimuth  $\theta_i$  with probability  $dn$

5.2. Randomly pick an angular position  $\varphi_i \in [0,360[$  ( $\varphi = 0$  being arbitrarily predefined)

Doing these previous steps yields one possible fragment configuration. That being said, no single configuration is perfectly representative of any shaped charge experiment. Steps 3 to 5 should therefore be repeated many times (followed by normalization with respect to the number of repetitions) in order to produce smooth distributions.

If, for a given scenario, a fragment table has to be filled, then all fragments in a configuration are sorted among possible domains in mass and azimuth distribution; fragments may only have some specific mass and azimuth as provided by the center of the domains<sup>4</sup>  $m_i^{dom}$  and  $\theta_i^{dom}$ . A velocity distribution has to be set up by defining a domain volume  $dv$  and incidentally  $v_i^{dom}$  values that will discretize the velocity distribution. The distributions are averaged over all repetitions. They would provide all necessary information required for SLAMS or GVAM (mass-velocity-direction-material)

Otherwise each fragment configuration may individually be used in an attack scenario in SLAMS; the final result could be the incapacitation in each annular zone (azimuth zone) and would be averaged over all repetitions and provided along with the standard error.

Since all tests were performed with a single kind of threat (66-mm shaped charge described in Section 2.1), the resulting model will be applicable only for this particular shaped charge. The expected values used throughout the procedure, *e.g.* mean total mass, mean total energy, thus implicitly understand a thickness dependence (as the parameterization was done over this parameter) but no dependences related to the threat itself.

---

<sup>4</sup> Note that the distributions do not have to be discretized with the same  $N^m$  and  $N^\theta$  values defined at step #2. Any values may be used.

### 5.3 Further improvements

The short model above, not yet implemented, is a simple way to provide a BAD table for more detailed studies as those made with SLAMS and GVAM. That being said, the procedure proposed above may easily be improved. The simplified methodology proposed above gathers the steps that should first be done in order to provide a functional BAD model fitted over main parameters. Once implemented, comparisons of yielded BAD tables should be done with experimental curves presented in previous chapters. Below follow a few observations and proposals (no particular order):

1. As most massive debris are expected to be ejected close to the jet axis, the average fragment mass  $\langle m \rangle$  should be correlated to the azimuth.
2. The actual procedure assumes no correlation between the velocity of the fragments and azimuth. This hypothesis should be verified.
3. If data with different shaped charges are available, it could be possible to add extra parameters in the fits and give some versatility to the model regarding the threat.
4. If data involving more target materials are available, extra parameters could be included in the fits in order to account for the material type and properties.
5. More data with different target plate thicknesses would smoothen the behaviour, and possibly extend the range of confidence in the thickness fits.
6. The angle of attack, *i.e.* the striking angle of the jet on the target, could become a parameter. However, it would complexify the steps in the process since the cloud of BAD would lose its axial symmetry and the fragment cones would be deformed. A reformulation of the topology of the problem would then be required.
7. So far, the mass and the energy (velocity) were attributed randomly disregarding the value of each other. Correlations between masses and energies should be verified. The determination of the velocities, as prescribed above, still bear a risk. Although there is a correlation between the velocity and the mass of a given fragment, undesirable situations such as attributing a very light fragment with a very high velocity could occur. Weighting attributed velocities with curves as those in Figures 9 and 10 (once normalized) could help ruling out such behaviours.
8. Only the conservation of the mass and energy were taken into account. Conservation of momentum could be introduced as well and used as guideline in the process of velocity attribution as well as azimuth angle such that no net radial momentum exists for single events.
9. The number of debris  $N$ , and the total mass  $M$  and total energy  $E$  of the fragments are computed in the procedure above as deterministic observations from equations 1, 2, 19 and 22. The nature of these variables is probabilistic. As data from many tests are available, it would be possible to build a distribution for each of these observations.

When building a fragment configuration, these parameters would be randomly chosen from their respective distribution.

10. Debris in, or close to the shaped charge jet path, were not accounted for because some of them could not be registered experimentally (they were lost in the hole created by the remnant of the jet). Actually, Figures 15, 16 and 33 should feature many fragments close to  $\theta = 0^\circ$ . Furthermore, fragments close to the jet path were not included in the total mass and energy calculation in order to avoid obtaining excessive values (because of the jet) and distribute large masses and energies to all fragments no matter their azimuth direction. Proposals 1 and 8 could help rehabilitate these fragments (close to  $\theta = 0^\circ$ ) without introducing any bias for the rest of the distribution. In its actual state, the resulting incapacitation from fragments in this narrow cone will be largely underestimated as this incapacitation should be very large. Computing total mass and energy for each azimuth zone could be a solution also. The latter would also fix points 1 and 2.
11. The cut-off value  $\theta_{cut}$  used in order to remove the jet fragments is arbitrary at some point. If this method has to be conserved, a more systematic way should be developed to retrieve contributions from the jet. That being said, the best solution would be to “measure” the jet remnant and to include them in the distributions (as opposed to the present situation where many pieces are unaccounted because of the large hole created in the witness pack). In this case one would mandatorily have to compute total mass and energy for each azimuth zone, as mentioned in point 9.

This page intentionally left blank.

## 6 Conclusion

---

This report compares the BAD generated by the penetration of a 66 mm shaped charge jet into Aluminium 5083 and Rolled Homogeneous Armour (RHA) steel.

RHA targets were tested for thicknesses between 1.6 mm and 127.5 mm. Aluminium 5083 targets were tested for thicknesses between 13 mm and 133 mm.

BAD was recorded using witness packs. The witness packs were analysed to find fragment positions, masses and velocities. A comparison between the two materials was made based on the total number of fragments, masses, velocities, and cumulative lethality for personnel subjected to the fragment cloud at a 60 cm standoff from the targets.

Looking at the number of fragments versus thickness, in all cases aluminium produced a lower number of behind armour debris by approximately 60%. A BAD model was adapted using the test results to predict BAD versus thickness for aluminium targets. The fragment mass and velocity distributions are similar for both materials, but since aluminium produces fewer fragments for the same thickness and areal density, the lethality of the debris cone is also more restrained for aluminium.

The behind armour debris characterisation and predictive model shown in this report can be used to estimate the vulnerability of personnel inside vehicles composed of those two materials when subjected to the shaped charge threat.

Improvements will be made to the behind armour analysis tool DeCaM to speed up the analysis. Additional experimental tests would help to refine the BAD versus thickness predictive model. The models developed are only valid for the specific 66-mm warhead used. Generalization could be made if tests with various shaped charge types, diameters and geometries were performed. Finally, all data processing was performed assuming that the BAD behaviour was the same either when a single plate or a stack of plates was used as target. Specific tests to evaluate the validity of that assumption could be performed.

This page intentionally left blank.

## 7 References

---

- [1] Baillargeon, Y., and Szymczak, M., Improvements to the Witness Pack Analysis System (WPAS), DREV TM 2000-208. Defence R&D Canada – Valcartier, 2001.
- [2] Merendino A., DiPersio R., Simon J., A method for predicting spallation from targets perforated by shaped Charge jets, BRL R1308, 1966.
- [3] STANAG 4589, ‘Static Testing of High-Explosive Munitions for Obtaining Fragment Spatial Distribution’, Edition 1, Military Agency for standardisation, 2000.
- [4] Sirois A., Baillargeon Y., New methods for lethality analysis of behind armour effects when using high performance mitigation systems (U), SECRET CEO, DRDC Valcartier TR 2009-130, September 2009.
- [5] Baillargeon, Y., Sirois, A., Behind-Armour Debris Produced by AM65 Shaped Charge for Thin RHA Targets at Normal and Oblique Impact Angles, SECRET, DRDC Valcartier TM 2004-364, March 2006.
- [6] Kokinakis, W., Sperrazza J., Criteria for Incapacitating Soldiers with Fragments and Flechettes, BRL R-1269, 1965
- [7] Sirois A., Baillargeon Y., Durocher R., Baseline on Karl Gustav FFV 551 performance and preliminary evaluation of behind armour effects on a light armoured vehicle hull (U), SECRET, DRDC Valcartier TM 2006-651, January 2008.
- [8] Dumas, S., “Survivability/Lethality Assessment and Modeling Software: an introduction to the ballistic module”, DRDC Valcartier TN 2007-444, December 2007.
- [9] Fortier C., “General Vulnerability Assessment Model (GVAM-III Version) User Manual”, DREV – TM-9436, February 1995.
- [10] Fortier C., “Shell for automating fragmentation runs \& Lethal Area calculations”, internal DRDC Valcartier document (file RMeFRAGSHELL.txt), 2000.



This page intentionally left blank.

## Annex A Total and average number of fragments

---

*Table A-1: Total number of fragments for the Al5083 targets*

Thickness (mm)	Areal density (kg/m <sup>2</sup> )	Total number of fragments	Average total number of fragments
13	35	363	408
13	35	303	
13	35	441	
13	35	523	
44,5	118	297	300
44,5	118	291	
44,5	118	312	
2 x 44,5 = 89	237	147	136
2 x 44,5 = 89	237	134	
2 x 44,5 = 89	237	127	
3 x 44,5 = 133.5	355	70	79
3 x 44,5 = 133.5	355	78	
3 x 44,5 = 133.5	355	88	

Table A-2: Total number of fragments for the RHA targets

Thickness (mm)	Areal density (kg/m <sup>2</sup> )	Total number of fragments	Average total number of fragments
1,6	13	715	748
1,6	13	780	
1,6	13	749	
6	47	1297	956
6	47	578	
6	47	992	
2 x 6 = 12	94	1306	1165
2 x 6 = 12	94	1307	
2 x 6 = 12	94	881	
3 x 6 = 18	141	1181	1087
3 x 6 = 18	141	1190	
3 x 6 = 18	141	1161	
1 x 18	141	1121	
1 x 18	141	905	
1 x 18	141	964	
25,5	200	945	981
25,5	200	1022	
25,5	200	977	
2 x 25,5 = 51	400	591	666
2 x 25,5 = 51	400	685	
2 x 25,5 = 51	400	721	
5 x 25,5 = 127,5	1001	58	156
5 x 25,5 = 127,5	1001	249	
5 x 25,5 = 127,5	1001	160	

DOCUMENT CONTROL DATA		
(Security classification of title, body of abstract and indexing annotation must be entered when the overall document is classified)		
1. ORIGINATOR (The name and address of the organization preparing the document. Organizations for whom the document was prepared, e.g. Centre sponsoring a contractor's report, or tasking agency, are entered in section 8.)  Defence R&D Canada – Valcartier 2459 Pie-XI Blvd North Quebec (Quebec) G3J 1X5 Canada	2. SECURITY CLASSIFICATION (Overall security classification of the document including special warning terms if applicable.)  UNCLASSIFIED (NON-CONTROLLED GOODS) DMC A REVIEW : GCEC JUNE 2010	
3. TITLE (The complete document title as indicated on the title page. Its classification should be indicated by the appropriate abbreviation (S, C or U) in parentheses after the title.)  Comparative analysis of behind armour debris from shaped charge impacts on aluminium and steel targets		
4. AUTHORS (last name, followed by initials – ranks, titles, etc. not to be used)  Alexandra Sirois; Yves Baillargeon; Alexandre Vallée; Guy Bergeron		
5. DATE OF PUBLICATION (Month and year of publication of document.)  June 2012	6a. NO. OF PAGES (Total containing information, including Annexes, Appendices, etc.)  68	6b. NO. OF REFS (Total cited in document.)  10
7. DESCRIPTIVE NOTES (The category of the document, e.g. technical report, technical note or memorandum. If appropriate, enter the type of report, e.g. interim, progress, summary, annual or final. Give the inclusive dates when a specific reporting period is covered.)  Technical Report		
8. SPONSORING ACTIVITY (The name of the department project office or laboratory sponsoring the research and development – include address.)  Defence R&D Canada – Valcartier 2459 Pie-XI Blvd North Quebec (Quebec) G3J 1X5 Canada		
9a. PROJECT OR GRANT NO. (If appropriate, the applicable research and development project or grant number under which the document was written. Please specify whether project or grant.)  12RF02	9b. CONTRACT NO. (If appropriate, the applicable number under which the document was written.)	
10a. ORIGINATOR'S DOCUMENT NUMBER (The official document number by which the document is identified by the originating activity. This number must be unique to this document.)  DRDC Valcartier TR 2012-063	10b. OTHER DOCUMENT NO(s). (Any other numbers which may be assigned this document either by the originator or by the sponsor.)	
11. DOCUMENT AVAILABILITY (Any limitations on further dissemination of the document, other than those imposed by security classification.)  Unlimited		
12. DOCUMENT ANNOUNCEMENT (Any limitation to the bibliographic announcement of this document. This will normally correspond to the Document Availability (11). However, where further distribution (beyond the audience specified in (11) is possible, a wider announcement audience may be selected.)  Unlimited		

13. **ABSTRACT** (A brief and factual summary of the document. It may also appear elsewhere in the body of the document itself. It is highly desirable that the abstract of classified documents be unclassified. Each paragraph of the abstract shall begin with an indication of the security classification of the information in the paragraph (unless the document itself is unclassified) represented as (S), (C), (R), or (U). It is not necessary to include here abstracts in both official languages unless the text is bilingual.)

This report aims at comparing the Behind Armour Debris (BAD) generated by the penetration of a shaped charge jet into two common vehicle armour materials: 5083 aluminium alloy and Rolled Homogeneous Armour (RHA) steel.

A statically detonated 66 mm shaped charge was used for the tests, which took place at the DRDC Valcartier exterior ranges. Targets were tested for thicknesses between 1.6 mm and 127.5 mm for RHA and 13 mm to 133 mm for 5083 aluminium alloy. Witness packs were used to record the behind armour debris, then scanned and analysed to obtain the behind armour debris distributions (fragment position, mass, velocity and lethality).

Comparing number of fragments versus thickness, aluminium has shown to produce about 60% less fragments around 13 mm. This difference gradually goes down to twice less for the thickest targets. Number of BAD in RHA reaches a peak around 12 mm (94 kg/m<sup>2</sup>) then decreases with thickness. For aluminium, targets thinner than 13 mm (35 kg/m<sup>2</sup>) were not tested, therefore the exact location of the peak in BAD is not visible in the test results, but from 13 mm to 127.5 mm, a gradual decrease in BAD was found. The fragment mass and velocity distributions are similar for both materials, but since aluminium produces fewer fragments, the lethality of the debris cone is smaller for aluminium. Predictive equations to numerically reproduce the behind armour debris distributions were developed based on the test results and are presented.

The behind armour debris characterisation data was consolidated into probability distribution models to be implemented into vulnerability-lethality tools. This was needed to estimate the vulnerability of personnel inside vehicles composed of any of those two materials when subjected to the shaped charge threat.

Les débris derrière le blindage résultant d'impacts de charges creuses dans deux matériaux fréquemment utilisés pour le blindage de véhicules (l'acier de blindage RHA et l'alliage d'aluminium 5083) sont comparés ici. Les tirs consistaient en des détonations statiques de charges creuses de 66 mm sur les sites d'essai de RDDC Valcartier. Les épaisseurs de cibles étaient entre 1,6 mm et 127,5 mm pour le RHA, et entre 13 mm et 133 mm pour l'aluminium. Des panneaux témoins ont été utilisés pour enregistrer les débris derrière le blindage puis scannés et analysés pour obtenir les distributions de débris (position, masse, vitesse et létalité des fragments).

L'analyse du nombre de fragments par rapport à l'épaisseur a montré que, dans tous les cas, l'aluminium produit environ 60 % moins de fragments que le RHA. Les distributions de masses et de vitesses sont similaires pour les deux matériaux, mais en produisant moins de fragments pour la même épaisseur, la zone de létalité produite par le cône de débris est plus petite pour l'aluminium. Des équations prédictives, qui serviront à reproduire numériquement les nuages de débris, ont été développées et sont présentées. Elles sont basées sur les résultats expérimentaux. La caractérisation des débris derrière le blindage a été consolidée en un modèle de distribution de probabilité afin d'être implémentée dans les outils de vulnérabilité-létalité. Cela est nécessaire pour pouvoir évaluer la vulnérabilité du personnel à l'intérieur de véhicules composés de ces matériaux lorsque exposés à un impact de charge creuse.

14. **KEYWORDS, DESCRIPTORS or IDENTIFIERS** (Technically meaningful terms or short phrases that characterize a document and could be helpful in cataloguing the document. They should be selected so that no security classification is required. Identifiers, such as equipment model designation, trade name, military project code name, geographic location may also be included. If possible keywords should be selected from a published thesaurus, e.g. Thesaurus of Engineering and Scientific Terms (TEST) and that thesaurus identified. If it is not possible to select indexing terms which are Unclassified, the classification of each should be indicated as with the title.)

Shaped charges, behind armour debris, vulnerability-lethality

## **Defence R&D Canada**

Canada's Leader in Defence  
and National Security  
Science and Technology

## **R & D pour la défense Canada**

Chef de file au Canada en matière  
De science et de technologie pour  
la défense et la sécurité nationale



[www.drdc-rddc.gc.ca](http://www.drdc-rddc.gc.ca)

